On Nuclear-Coupled Thermal-Hydraulic Instability Analysis of Super-Critical-Light-Water-cooled-Reactor (SCLWR)

Subhanker Paul[1,*]

Department of Energy and Process Engineering

Norwegian University of Science and Technology (NTNU), Norway

Abstract

The nonlinear stability analysis of a supercritical light water reactor (SCLWR) is presented using a nuclear-coupled thermal-hydraulic reduced-order model. The analytical model is developed by coupling 1. the point-kinetics equations with one group of delayed neutrons, 2. the fuel heat transfer and 3. a 1-D reduced order model which represents the heat absorption phenomenon during the coolant flow. Unlike the existing studies, which are limited to linear stability analysis, the primary objective of the work is to present the detailed nonlinear dynamics of the SCLWR system. The said goal is achieved at two levels. The first level is the linear stability analysis wherein the linear stability boundaries are shown in two sets of parameter space namely the two intrinsic reactivity feedbacks (Doppler reactivity feedback and density reactivity feedback) and the pseudo-phase-change number and pseudo subcooling number. The parametric effects show the sensitivity of the linear stability boundaries with the system parameters. In the second level, to discuss the nonlinear characteristics of the system, two types of Hopf bifurcations (subcritical and supercritical) are studied with the help of first Lyapunov coefficients of the system. Multiple numerical simulations are performed to verify the resultant limit cycle behavior associated with these bifurcations. Moreover, the occurrence of the generalized Hopf bifurcation is shown which represents the bifurcation between the subcritical Hopf and the supercritical Hopf regions. Further, inside the stable region of the linear stability boundary, the saddle-node bifurcation is found which represents the location of the turning point and the threshold of the globally stable region of the system.

Keywords: super-critical-light water reactor, linear stability, nonlinear stability,

subcritical Hopf, supercritical Hopf, generalized Hopf, saddle node bifurcation, globally stable region

1. Introduction

Modeling and analysis of Super-Critical-Light-Water cooled Reactors (SCLWRs) are of paramount interest to researchers for several decades. This is due to the large thermal efficiency of SCLWRs compared to light water reactors. The core cooling system of an SCLWR is a once-through direct cycle in which the coolant does not boil and flows directly to the turbine. This also reduces the overall maintenance cost of the reactor as compared to light water reactors, where the turbine is more susceptible to wear and tear. The core coolant flow rate is approximately one-eighth of that of a Boiling-Water-Reactor (BWR) (Dobashi et al., 1997) because of the high enthalpy difference and no recirculation. In SCLWR, since the coolant does not undergo a phase-change when it crosses the pseudo-critical point; hence, it can operate at a very high temperature without triggering the departure from nucleate boiling phenomenon. However, when the coolant crosses the pseudo-critical point, it's density decreases by a large extent (e.g. In the U.S. reference SCLWR, the density decreases from $780 kg/m^3$ to $90 kg/m^3$). This large decrease in density coupled with nuclear feedbacks raises concern to flow instabilities in an SCLWR.

Till now, several studies have been carried out to analyze these instabilities in SCLWRs. The flow instabilities have been reported by Chatoorgoon (2001). He studied the steady and nonlinear stability behavior of a natural circulation loop with supercritical water acting as a coolant. Yang and Zavaljevski (2003) has presented the single channel stability of the U.S. reference design of SCLWR. Yang and Zavaljevski (2003) analyzed the stability behavior of the U.S. reference SCLWR with a linear model. Further, the study was extended by Yang and Zavaljevski (2005) to include the effect of water rod heating. Several other studies have been presented by Zhao et al. (2004a,b); Zhao (2005); Zhao et al. (2006, 2007) with

*Corresponding author
Email address: imsubhanker@gmail.com (Subhanker Paul)
[1]Permanent address: Amity Institute of Nuclear Science and Technology (AINST), Amity University Uttar Pradesh (AUUP), India, 201303

matrix multiplication method to analyze the stability characteristics of the U.S. reference SCLWR and supercritical CO_2 cooled reactors. Later, Jain and Rizwan-uddin (2008) investigated the flow instabilities in a supercritical CO_2 natural circulation loop. Moreover, Sharma et al. (2009, 2010) also presented the steady-state and linear stability of an SCLWR natural circulation loop.

It should be noted that, although a plethora of literature provided stability analyses of SCLWRs, they are limited to linear stability analyses only. These linear stability analyses only provide the system behavior in the vicinity of the stability boundaries and are valid for small perturbations in the system. However, recent studies on similar dynamical systems by Pandey and Singh (2016, 2017); Verma et al. (2018); Rahman and Singh (2018) reveal that the dynamical system like nuclear reactors possess various other stability behavior when investigations are made in a wide range of parametric space away from the linear stability threshold region. These behaviors are dominantly known as nonlinear stability characteristics which provide very good information about the system behavior with large perturbations. Moreover, most of the literature do not present the detailed stability analyses of an SCLWR in the wide ranges of various reactivity feedbacks, which couples the thermal hydraulic and neutron generation inside a reactor core.

Considering the extreme operating conditions associated with an SCLWR and the possible occurrence of nonlinear stability behavior similar to the BWRs, which may trigger undesired events like power oscillations leading to a system failure, it is essential to present a detailed investigation of the linear and nonlinear stability of the SCLWR.

With an aim to suffuse the mentioned knowledge-gap, in this work, a nuclear-coupled thermal-hydraulic reduced order model of an SCLWR is presented. To represent the neutron balance inside the reactor core, a point reactor kinetic model is used. To represent the thermal-hydraulic, a two-zone reduced order model is used. The concept of reduced-order-model has proven its' capability to model similar systems in earlier studies (Paul and Singh, 2014a,b, 2015, 2017a,b; Dokhane et al., 2007a,b). The adoption of the two-zone reduced order model makes the analyses convenient, as in the one hand; it provides results close to realistic conditions, on the other hand, the use of linear approximations makes the system

equations simpler. The two intrinsic reactivity feedbacks namely Doppler and the density provide the coupling between the neutron balance and the thermal-hydraulic of the said dynamical system.

The primary objective of this work is to delineate the comprehensive nonlinear stability of an SCLWR. The linear and nonlinear stability of the dynamical system are discussed in two sets of parameter planes; first the Doppler and density coefficient of reactivity and second; the pseudo-phase-change number and pseudo-subcooling number. This study reveals the occurrence of various types of bifurcations namely; subcritical Hopf, supercritical Hopf, Generalized Hopf, and saddle-node bifurcation. In addition, the bistable region and globally stable region are also shown.

2. Mathematical Model

In this section, a simplified mathematical model for a forced circulation SCLWR is developed. The model couples the neutronics with a thermal-hydraulic reduced order model for the coolant. The SCLWR lattice cell is considered as a single vertical channel with the fuel at its center. The whole mathematical model of the SCLWR is developed in three sections namely 1. Neutronics modeling, 2. Fuel heat transfer modeling, and 3. Coolant thermal-hydraulic modeling. It should be noted that all the symbols used to write the equations are explained in the Nomenclature.

2.1. Neutronics Modeling

The neutron balance inside the SCLWR core is represented by the point-kinetics equations with one group of delayed neutrons as

$$\frac{dN^*(\tau^*)}{d\tau^*} = \frac{R(\tau^*) - \beta}{\Lambda^*} N^*(\tau^*) + \lambda^* C^*(\tau^*) \tag{1}$$

and

$$\frac{dC^*(\tau^*)}{d\tau^*} = \frac{\beta}{\Lambda^*} N^*(\tau^*) - \lambda^* C^*(\tau^*) \tag{2}$$

The net reactivity $R(\tau^*)$ appearing in Eq. 1 has three components namely, steady-state reactivity, reactivity due to external sources and feedback reactivity. Since we represent the neutron balance inside the core by a source free point kinetics model, hence the reactivity due to external sources are zero. In addition, the SCLWR system being an autonomous system, the steady-state reactivity is taken as zero. Thus, the net reactivity $R(\tau^*)$ consists of only feedback reactivities. Although there are several components of feedback reactivities inside a reactor core, for simplicity, the present model limits its' scope by considering only the intrinsic dynamic and hence only the intrinsic reactivity feedbacks namely Doppler reactivity and density reactivity are considered. Assuming a linear model, the net reactivity $R(\tau^*)$ is written as,

$$R(\tau^*) = R_D(\tau^*) + R_d(\tau^*) = \alpha_f^*(T_F^*(\tau^*) - T_{F0}^*(\tau^*)) + \alpha_d^*(\rho_{avg}^*(\tau^*) - \rho_{avg0}^*) \tag{3}$$

2.2. Fuel Heat Transfer Modeling

The fuel heat balance equation is written in analogy to that written for BWRs (Verma et al., 2018) as,

$$\rho_F^* C_{PF}^* A_c^* \frac{dT_F^*(\tau^*)}{d\tau^*} = A_c^* q'''^*(\tau^*) - P_h^* q''^*(\tau^*) \tag{4}$$

where the volumetric heat generation rate $q'''^*(\tau^*)$ is directly proportional to the neutrons generated inside the reactor core and thus

$$q'''^* = C_q^* N^*(\tau^*) \tag{5}$$

where C_q^* is the proportionality constant between the volumetric heat generation rate and the neutrons generated inside the core.
Assuming a uniform heat flux along the length of the whole fuel element, the heat flux q''^* is written as,

$$q''^* = H^*(T_F^*(\tau^*) - T_{pc}^*) \tag{6}$$

where H^* represents the overall heat transfer coefficient. It is calculated by the relation given in Eq. 7 (Yi et al., 2004a,b). Note that, to write the Eq. 6, the whole coolant inside the flow

channel is assumed to be at uniform temperature T^*_{pc}. To model a reasonably simple case for the SCLWR and to present the nonlinear dynamics; such assumption has been made. Although the temperature variation of the coolant along the length of the flow channel can be considered for representing the system dynamics close to realistic conditions, for the sake of simplicity the variation of the coolant temperature along the length of the flow channel is neglected.

$$H^* = \frac{N_u * k^*}{D^*_e} \tag{7}$$

$$N_u = 0.015 * Re^{0.85} * Pr^y \tag{8}$$

The parameter y is given by:

$$y = 0.69 - \frac{81000}{200G^{*1.25}} + \left(-8.7 * 10^{-8} - \frac{0.65}{200G^{*1.25}} \right) \tag{9}$$

The Eq. 4 can now be written as

$$\rho^*_F C^*_{PF} A^*_c \frac{dT^*_F(\tau^*)}{d\tau^*} = A^*_c q'''^*(\tau^*) - P^*_h H^*(T^*_F(\tau^*) - T^*_{pc}) \tag{10}$$

By choosing the non-dimensional variables given in Appendix A, the set of equations (Eqs. 1, 2, and 10) are written in the non-dimensional form as;

$$\frac{dx_1}{dt} = \Lambda \Big(x_1 + x_2 + (1 + x_1)(a_f x_3 + a_d(\rho_{avg}(t) - \rho_{avg,0})) \Big) \tag{11}$$

$$\frac{dx_2}{dt} = \lambda(x_1 - x_2) \tag{12}$$

$$\frac{dx_3}{dt} = \xi_1 x_1 - \xi_2 x_3 \tag{13}$$

It is worth noting that, in the above set of equations the term $\rho_{avg}(t)$ provides the coupling between the neutron kinetics and the thermal-hydraulic of the dynamical system. The term $\rho_{avg}(t)$ represents the average density of the coolant during its flow through the channel. The mathematical expression to calculate this term is explained in the next section.

2.3. Coolant Thermal-Hydraulic Modeling

The thermal-hydraulic model of the SCLWR coolant flow system is developed by assuming a 1-D axial flow. The three basic conservation PDEs of mass, energy, and momentum are used to define the flow phenomenon. Although, in reality; the flow system of the SCLWR contains various flow driving components and phenomena, including all those phenomena in this analysis will increase the complexity of the model. In addition, since the primary objective of the present work is to delineate the nonlinear stability behavior of the system, hence for the sake of parity; all such phenomena are disregarded. To develop the model some simplifying assumptions are made in analogy to that used for subcritical fluid flow systems (Singh et al., 2018).

Assumptions used in this model are as follows,

1. The system pressure remains constant.
2. Input heat flux is uniform along the length of the channel.
3. $\frac{\partial P}{\partial t}$ term in the energy conservation equation is neglected.

Using the above assumptions, the one-dimensional mass, momentum, and energy balance equations are written as:

$$\frac{\partial \rho^*}{\partial \tau^*} + \frac{\partial (\rho^* w^*)}{\partial z^*} = 0 \tag{14}$$

$$\rho^* \frac{\partial w^*}{\partial \tau^*} + \rho^* w^* \frac{\partial w^*}{\partial z^*} = -\frac{\partial P^*}{\partial z^*} - \rho^* g^* - [\frac{f^*}{D_h^*} + 2K_{in}^* \delta_d^*(z^*) + 2K_{exit}^* \delta_d^*(z^* - L^*)] \frac{\rho^* w^{*2}}{2} \tag{15}$$

$$\rho^* \frac{\partial h^*}{\partial \tau^*} + \rho^* w^* \frac{\partial h^*}{\partial z^*} = \frac{q''^* P_h^*}{A_c^*} \tag{16}$$

In the momentum equation (Eq. 15), the two functions δ_d^* represent the dimensional Dirac delta functions centered at the channel inlet and the exit respectively. These functions provide a mathematical formulation of the localized pressure drops at the inlet and the exit of the channel.

Using the established non-dimensional parameters given by Ambrosini and Sharabi (2008); Ambrosini (2009), and making use of the relations given in Appendix A, the aforementioned set of conservation PDEs are converted into following non-dimensional form as:

$$\frac{\partial \rho}{\partial t} + \frac{\partial (\rho w)}{\partial z} = 0 \tag{17}$$

$$\rho \frac{\partial w}{\partial t} + \rho w \frac{\partial w}{\partial z} = -\frac{\partial P}{\partial z} - \rho g - [N_f + K_{in}\delta_d(z) + K_{exit}\delta_d(z-L)]\rho w^2 \tag{18}$$

$$\rho \frac{\partial h}{\partial t} + \rho w \frac{\partial h}{\partial z} = N_{tpc}(x_3 + 1 - \Delta) \tag{19}$$

Note that, the non-dimenional parameter N_{tpc} is directly proportional to the steady-state fuel rod temperature T^*_{F0} which defines the wall heat flux q''^*_0. The term N_{tpc} is defined as:

$$N_{tpc} = \frac{H^* T^*_{F0} P^*_h \beta^*_{pc} L^*_{ch}}{A^*_c \rho^*_{pc} C^*_{pc} W^*_0} \tag{20}$$

The Eq. 20 shows that, a change in N_{tpc} changes the T^*_{F0} which eventually changes the steady-state neutron density (N^*_0, by using Eq. 4, and 5) inside the reactor core. These inter-relations provide perfect coupling between the neutron kinetic and the thermal hydraulic phenomena.

Since the density of a supercritical fluid changes significantly as it crosses the pseudo-critical point, hence in the present work the flow channel is modeled in two zones (Fig. 1). In the lower section (where the temperature of the fluid is below the pseudo-critical temperature) the fluid density does not decrease significantly as it absorbs heat. In the upper section; after crossing the pseudo-critical point (the temperature of the fluid becomes higher than the pseudo-critical temperature), the density of the fluid decreases rapidly. Hence, the lower section is called as Heavy fluid zone, and the upper section is called as Light fluid zone.

2.3.1. Equations for the heavy fluid zone

To develop the reduced order model of the PDEs (Eq. 17,19), the enthalpy, density and velocity of the supercritical water are spatially approximated as:

$$h(z,t) = h_{in} + a_1(t)z \tag{21}$$

$$\rho(z,t) = \frac{1}{\frac{1}{\rho_{in}} + b_1(t)z} \tag{22}$$

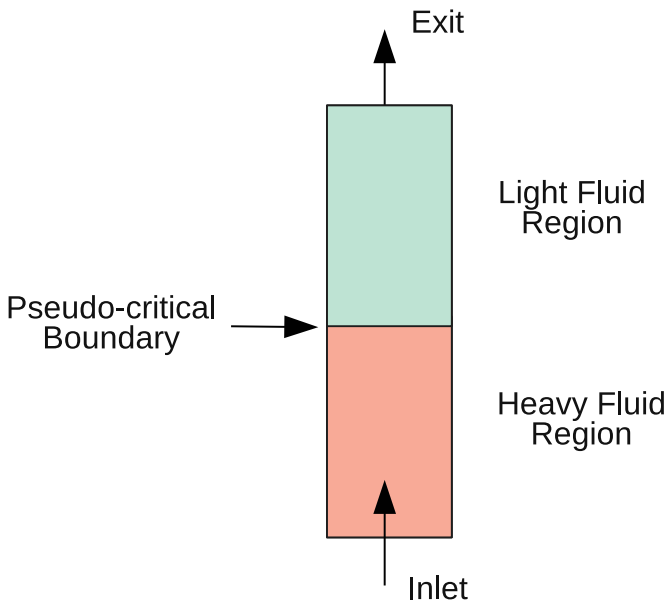

Figure 1: Schematic view of flow channel

$$w(z,t) = w_{in}(t) + A_1 N_{tpc}(x_3 + 1 - \Delta)z \tag{23}$$

where the detailed justification for using the above-mentioned approximations are given in Appendix B. The coefficients $a_1(t)$ and $b_1(t)$ provides the time dependency of the enthalpy and the density respectively. It should be noted that, since spatial approximations are used to identify the solutions of the conservation PDEs, it is necessary to minimize the error over the respective region. Hence, using the equations (Eq. 21, 22, 23), weighted residual method is applied to the energy and mass conservation PDEs (Eq. 17, 19) and thus we get the set of coupled nonlinear ODEs as:

$$\int_0^{L_{pc}(t)} (\frac{da_1}{dt} z + \rho(z,t) w(z,t) a_1(t) - N_{tpc}(x_3 + 1 - \Delta))\psi_1(z) dz = 0 \tag{24}$$

$$\int_0^{L_{pc}(t)} (\frac{\partial \rho(z,t)}{\partial t} + \frac{\partial}{\partial z}[\rho(z,t) w(z,t)])\psi_2(z) dz = 0 \tag{25}$$

where $\psi_1(z)$ and $\psi_2(z)$ are the weighting functions (chosen as unity). The pseudo-critical boundary ($L_{pc}(t)$) is given by,

$$L_{pc}(t) = \frac{h_{pc} - h_{in}}{a_1(t)} = \frac{N_{spc}}{a_1(t)} \tag{26}$$

Simplifying the equations (Eq. 24, 25), we get the coupled nonlinear ODEs as,

$$\frac{da_1(t)}{dt} = \Phi_1(t) \tag{27}$$

$$\frac{db_1(t)}{dt} = \Phi_2(t) \tag{28}$$

The detailed expressions of the functions $\Phi_1(t)$ and $\Phi_2(t)$ are given in Appendix D.

2.3.2. Equations for the light fluid zone

Similar to the heavy fluid zone, the enthalpy, density and velocity of the supercritical water in the light fluid zone are approximated as:

$$h(z,t) = h_{pc} + a_2(t)(z - L_{pc}(t)) \tag{29}$$

$$\rho(z,t) = \frac{1}{\frac{1}{\rho_{pc}(t)} + b_2(t)(z - L_{pc}(t))} \tag{30}$$

$$w(z,t) = w_{pc}(t) + A_2 N_{tpc}(x_3 + 1 - \Delta)(z - L_{pc}(t)) \tag{31}$$

Following the same weighted residual procedure as done in section 2.3.1, the energy and mass conservation PDEs are converted into coupled nonlinear ODEs as:

$$\frac{da_2(t)}{dt} = \Phi_3(t) \tag{32}$$

$$\frac{db_2(t)}{dt} = \Phi_4(t) \tag{33}$$

The detailed expressions of the functions $\Phi_3(t)$ and $\Phi_4(t)$ are given in Appendix D.

2.3.3. Equation for the fluid velocity

The equation for the fluid velocity; which governs the inlet flow rate of the coolant during the flow oscillations is obtained by integrating the momentum conservation equation (Eq. 18) over the two zones. The spatially approximated relations of the flow variables (density and velocity, Eq. 22, 23, 30, 31) are used to in the momentum conservation equation during the integrations.

Integrating the momentum conservation PDE in the heavy fluid zone, we get the pressure drop across this zone as:

$$\Delta P_{heavy} = \Phi_5(t) \tag{34}$$

Similarly, integrating the momentum conservation PDE in the light fluid zone, we get the pressure drop across this zone as:

$$\Delta P_{light} = \Phi_6(t) \tag{35}$$

Equating the sum of the two pressure drops mentioned above to a constant external pressure drop ΔP_{ext}, we get the ODE for the inlet velocity as:

$$\frac{dw_{in}(t)}{dt} = \Phi_7(t) \tag{36}$$

The detailed expressions of the functions $\Phi_5(t)$, $\Phi_6(t)$, and $\Phi_7(t)$ are given in Appendix D. It is worth noting that, the assumption of constant external pressure drop is reasonable because it replicates the realistic condition inside a reactor core. Inside the core of a typical nuclear reactor, a large number of coolant channels exist (typically of the order of 10^3). In these kind of designs where the coolant flow across multiple parallel channels, if one channel experience disturbance in its flow condition, the rest of the channels inside the core can easily fix the pressure drop across the single channel due to a large bypass effect. Hence, to derive the ODE for inlet velocity of the coolant, a constant external pressure drop is considered.

3. Representation of the SCLWR Dynamical System

Following the derivations done in the previous section 2, the SCLWR dynamical system is represented by the set of eight coupled nonlinear ODEs as:

$$\frac{dx_1}{dt} = \Lambda\Big(- x_1 + x_2 + (1 + x_1)(a_f x_3 + a_d(\rho_{avg}(t) - \rho_{avg,0}))\Big) \tag{37}$$

$$\frac{dx_2}{dt} = \lambda(x_1 - x_2) \tag{38}$$

$$\frac{dx_3}{dt} = \xi_1 x_1 - \xi_2 x_3 \tag{39}$$

$$\frac{da_1(t)}{dt} = \Phi_1(t) \tag{40}$$

$$\frac{db_1(t)}{dt} = \Phi_2(t) \tag{41}$$

$$\frac{da_2(t)}{dt} = \Phi_3(t) \tag{42}$$

$$\frac{db_2(t)}{dt} = \Phi_4(t) \tag{43}$$

$$\frac{dw_{in}(t)}{dt} = \Phi_7(t) \tag{44}$$

A close inspection of the above system of ODEs reveal that, the variables x_1, x_2, and x_3 represent the fluctuations around the steady state values of neutron density, delayed neutron precursor density, and fuel rod temperature respectively. The variables a_1, b_1, a_2, b_2, and w_{in} represent the time dependent component of the enthalpy, density and the coolant inlet velocity.

During the steady-state operation of the SCLWR, the values of x_1, x_2, and x_3 become zero. Whereas, the values of a_1, b_1, a_2, b_2, and w_{in} are:

$$a_{1,0} = \frac{N_{tpc}}{\rho_{in}}(1 - \Delta) \tag{45}$$

$$b_{1,0} = A_1\frac{N_{tpc}}{\rho_{in}}(1 - \Delta) \tag{46}$$

$$a_{2,0} = \frac{N_{tpc}}{\rho_{in}}(1 - \Delta) \tag{47}$$

$$b_{2,0} = A_2 \frac{N_{tpc}}{\rho_{in}}(1-\Delta) \tag{48}$$

$$w_{in,0} = 1 \tag{49}$$

Hence, to make the representation of the dynamical system uniform across all the variables; suitable change of variables around the steady-state values are applied to a_1, b_1, a_2, b_2, and w_{in} as:

$$x_4(t) = a_1(t) - a_{1,0} = a_1(t) - \frac{N_{tpc}}{\rho_{in}}(1-\Delta) \tag{50}$$

$$x_5(t) = b_1(t) - b_{1,0} = b_1(t) - A_1\frac{N_{tpc}}{\rho_{in}}(1-\Delta) \tag{51}$$

$$x_6(t) = a_2(t) - a_{2,0} = a_2(t) - \frac{N_{tpc}}{\rho_{in}}(1-\Delta) \tag{52}$$

$$x_7(t) = b_2(t) - b_{2,0} = b_2(t) - A_2\frac{N_{tpc}}{\rho_{in}}(1-\Delta) \tag{53}$$

$$x_8(t) = w_{in}(t) - w_{in,0} = w_{in}(t) - 1 \tag{54}$$

The variables x_4, x_5, x_6, x_7, and x_8 represent the fluctuations around the steady state values of the time dependent coefficients of a_1, b_1, a_2, b_2, and w_{in}. The steady-state values of the variables x_4, x_5, x_6, x_7, and x_8 now become zero, thus it makes the representation of the dynamical system of SCLWR uniform. With these change in variables, the dynamical system of SCLWR now become:

$$\frac{dx_1}{dt} = \Lambda\Big(- x_1 + x_2 + (1+x_1)(a_f x_3 + a_d(\rho_{avg}(t) - \rho_{avg,0}))\Big) \tag{55}$$

$$\frac{dx_2}{dt} = \lambda(x_1 - x_2) \tag{56}$$

$$\frac{dx_3}{dt} = \xi_1 x_1 - \xi_2 x_3 \tag{57}$$

$$\frac{dx_4}{dt} = \Phi_8(t) \tag{58}$$

$$\frac{dx_5}{dt} = \Phi_9(t) \tag{59}$$

$$\frac{dx_6}{dt} = \Phi_{10}(t) \tag{60}$$

$$\frac{dx_7}{dt} = \Phi_{11}(t) \tag{61}$$

$$\frac{dx_8}{dt} = \Phi_{12}(t) \tag{62}$$

The detailed expressions for all the functions are given in Appendix D

4. Linear Stability Analysis (First Level): Search for Hopf Bifurcation

The first step which sets the platform to carry detailed nonlinear stability analysis of any dynamical system is Linear stability analysis. This provides information about the onset of instabilities of a dynamical system under the influence of small perturbations in its normal (steady) operating conditions. To perform the linear stability analysis, the set of ODEs are linearized around the equilibrium solution (steady-state) of the dynamical system. The linearized equation is known as characteristic equation. Then, the roots of the characteristic equation are studied to determine the linear stability behavior. To perform the linear stability analysis, the dynamics of the SCLWR is written in a generalized state-space form as:

$$\dot{\overrightarrow{\mathrm{X}}} = F\left(\overrightarrow{\mathrm{X}}(t), \eta\right) \tag{63}$$

where $\overrightarrow{\mathrm{X}}(t) = (x_1, x_2, x_3, x_4, x_5, x_6, x_7, x_8)^T$ is the set of state variables and η is the set of design and operating parameters. Since the steady-state values of all the state variables are zero, hence performing Taylor series expansion around the steady-state values and dropping the higher order terms (by considering small perturbation), Eq. 63 can be written as:

$$\delta\dot{\overrightarrow{\mathrm{X}}} = J\left(\overrightarrow{\mathrm{X}_0}, \eta\right)\delta\overrightarrow{\mathrm{X}} \tag{64}$$

Here, J is the Jacobian obtained after linearizing the above system of ODEs. To determine the linear stability characteristics, the eigenvalues of this Jacobian are monitored across the mentioned parameter spaces of $N'_{tpc} - N_{spc}$ and $a_f - a_d$. Since an oscillatory system posses complex eigenvalues, the real and imaginary part of the eigenvalue determines the stability and frequency of oscillation. A set of parameter will be qualified for a stable state (damped oscillation) if real parts of all the eigenvalues of this Jacobian become negative. However,

the system will be unstable (growing oscillation) if at-least one real part of the eigenvalues is positive and the corresponding set of parameters will be known as the unstable state. The set of parameters at which the real part of the complex eigenvalue become zero is known as the linear stability threshold. At this point, the system has pure imaginary eigenvalues and shows self-sustained oscillations with constant amplitude and frequency. The loci of all such thresholds represents the linear stability boundary (Hopf bifurcation boundary). The criteria for occurrence of Hopf bifurcation is given in Appendix C. Mathematically, the linear stability thresholds followed by the linear stability boundary are generated by solving the following set of equations.

$$Real\Big(Det(J - \iota\omega I)\Big) = 0$$
$$Imag\Big(Det(J - \iota\omega I)\Big) = 0$$

where $\iota = \sqrt{-1}$ and I is the identity matrix. The SCLWR system has four independent operating parameters namely, 1. Pseudo phase change number ($N'_{tpc} = \frac{N_{tpc}}{\rho_{in}}$), 2. Pseudo subcooling number (N_{spc}), 3. Doppler coefficient of reactivity (a_f), and 4. Density coefficient of reactivity (a_d). The linear stability boundaries are plotted by varying two parameters at a time keeping the rest of the two parameters fixed. The stability boundaries thus obtained are shown in Fig. 2. The various design parameters used to obtain these stability boundaries Dobashi et al. (1997) are given in Table 1.

In Fig. 2, the Hopf bifurcation boundary (representing the linear stability) is depicted by blue lines while the static instability boundary is shown by a red line (detailed explanation of static instability is given in Appendix C). In Figure 2a a typical L-fold nature of the stability map is observed as evident from the existing literature. From Figure 2b it is seen that the SCLWR system is stable when operated at positive density coefficient of reactivities (a_d). This is in agreement with the real case, as in real operating conditions, the SCLWR is operated with positive density coefficient of reactivities. It is also observed that Fig. 2b predicts a stable region of operation for some positive Doppler coefficient of reactivities

Table 1: Characteristics of SCLWR with single tube water rods (with orifices and channel boxes)

Thermal/electric power (MW)	2490/1013
Thermal efficiency (%)	40.7
Pressure (MPa)	25
Fuel assembly	
Fuel/fuel rod dia./pitch (cm)	UO_2/0.80/0.95
Cladding/thickness (cm)	SSs/0.046
Number of fuel/water/control rods	258/30/9
Uranium enrichment, upper/middle/lower (%)	6.41/5.22/4.66
Number of fuel rods containing gadolinia	31
Gadolinia concentration, upper/ middle/ lower (wt%)	2.1/3.1/4.3
Number of fuel assemblies	163
Average Power Density (MW/m^3)	106
Discharge burnup ($GW_{d/t}$)	45
Refueling period (days)	400
Feedwater flow rate (kg/s)	2314
Coolant inlet/outlet temperature (°C)	324/397
Core height/dia. (m)	3.70/2.84
Reactor pressure vessel thickness (cm)	32.2
Total peaking factor (for design)	2.50
Calculated total/axial/radial/local peaking factors	2.31/1.58/1.26/1.16
Doppler coefficient at HFP (pcm/K)	-2.4
Coolant density coefficient (dk/k/[g/cm^3])	0.45
Other parameters assumed (due to unavailability)	
Inlet/Exit loss coefficient (K_{in}/K_{exit})	0
Friction number (N_f)	4.34
λ^* (s^{-1})	0.075
Λ^* (s)	$22 * 10^{-5}$
β	0.003

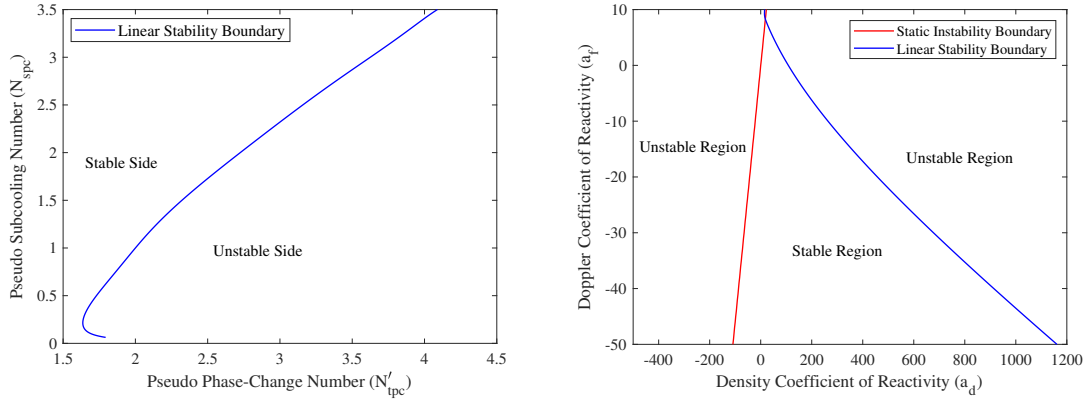

(a) (b)

Figure 2: Stability diagrams of SCLWR in (a) $N'_{tpc} - N_{spc}$ plane and (b) $a_d - a_f$ plane

(a_f), provided the density coefficient of reactivity is positive. Moreover, as the value of a_f is increased, it shrinks the stable operation region rapidly. The highest possible value of a_f for stable operation of the SCLWR with the chosen design parameters is found to be 10. In short, it is concluded from Figure 2 that increase in N_{spc} will stabilize the system, whereas increase in N'_{tpc} and a_d will drive the system towards unstable region.

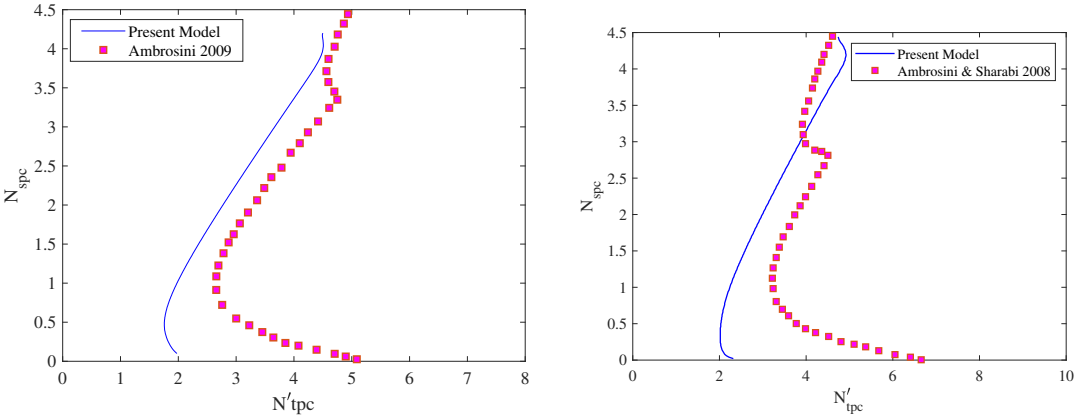

(a) (b)

Figure 3: Comparison of stability boundaries obtained by the present model with the studies by Ambrosini and Sharabi (2008); Ambrosini (2009)

To validate the model predictions, the linear stability boundaries obtained with the present model are compared with the results of Ambrosini and Sharabi (2008); Ambrosini

(2009) and significant agreements are observed. The discrepancies observed between the present model and the existing literature is due to the numerical model adopted. Since the present model is developed by assuming the channel to be composed of three nodes (two-regions: heavy fluid region and light fluid region), the model results differ to that of Ambrosini and Sharabi (2008); Ambrosini (2009) where the authors considered 48 nodes for the analyses. Moreover, from Fig. 4 it is observed that the stability boundaries obtained using the present model also depend on the parameters (A_1 & A_2) which capture the drastic change in the density along the length of the flow channel.Thus, these comparisons provided a level of confidence to carry a detailed stability analysis of the SCLWR dynamical system.

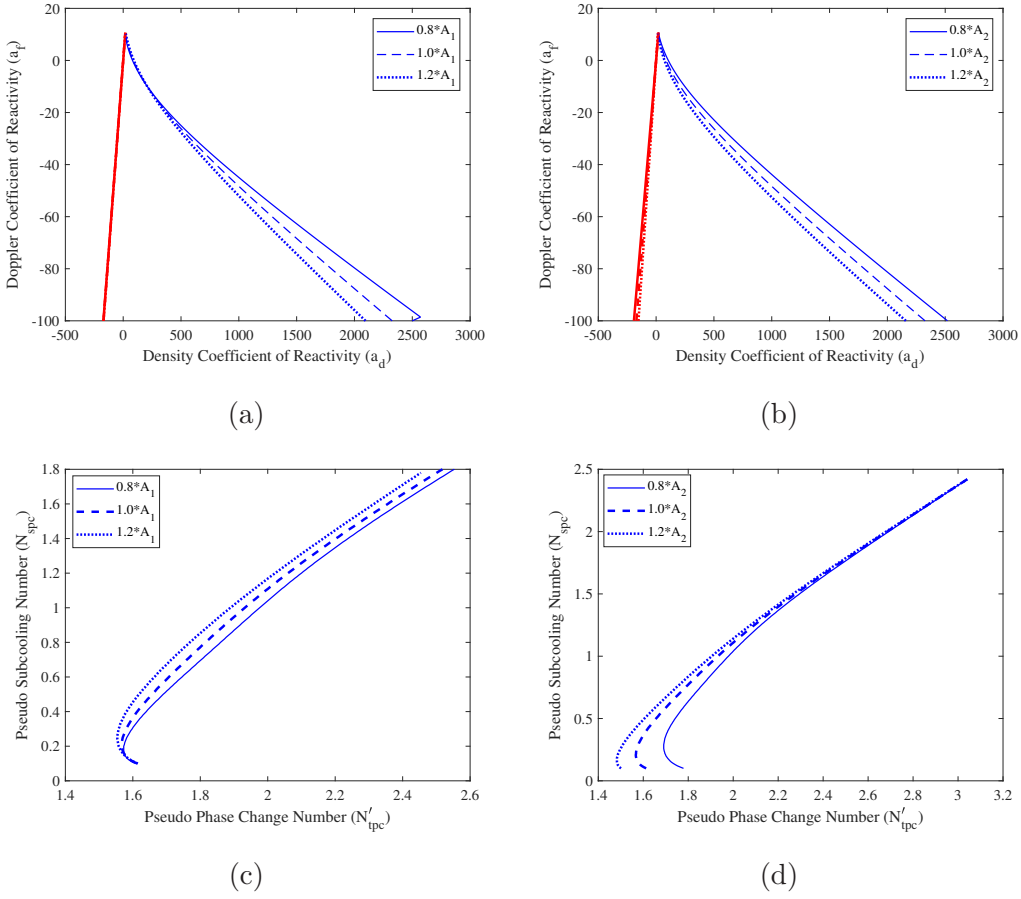

Figure 4: Shows that by changing the parameters which capture the variation of the density along the length of the flow channel; the stability boundaries change their position. This indicates that to obtain a better accuracy of the results, one can increase the number of nodes along the length of the channel to capture the actual density variation.

5. Parametric Effects on Linear Stability

In this section, the effect of some key design (K_{in} and K_{exit}) and operating parameters (a_d, a_f, N'_{tpc}, and N_{spc}) on the linear stability characteristics of the system are shown. for this purpose stability boundaries are plotted first in reactivity plane ($a_d - a_f$) and second in heat flux plane ($N'_{tpc} - N_{spc}$) keeping the rest of the parameters fixed.

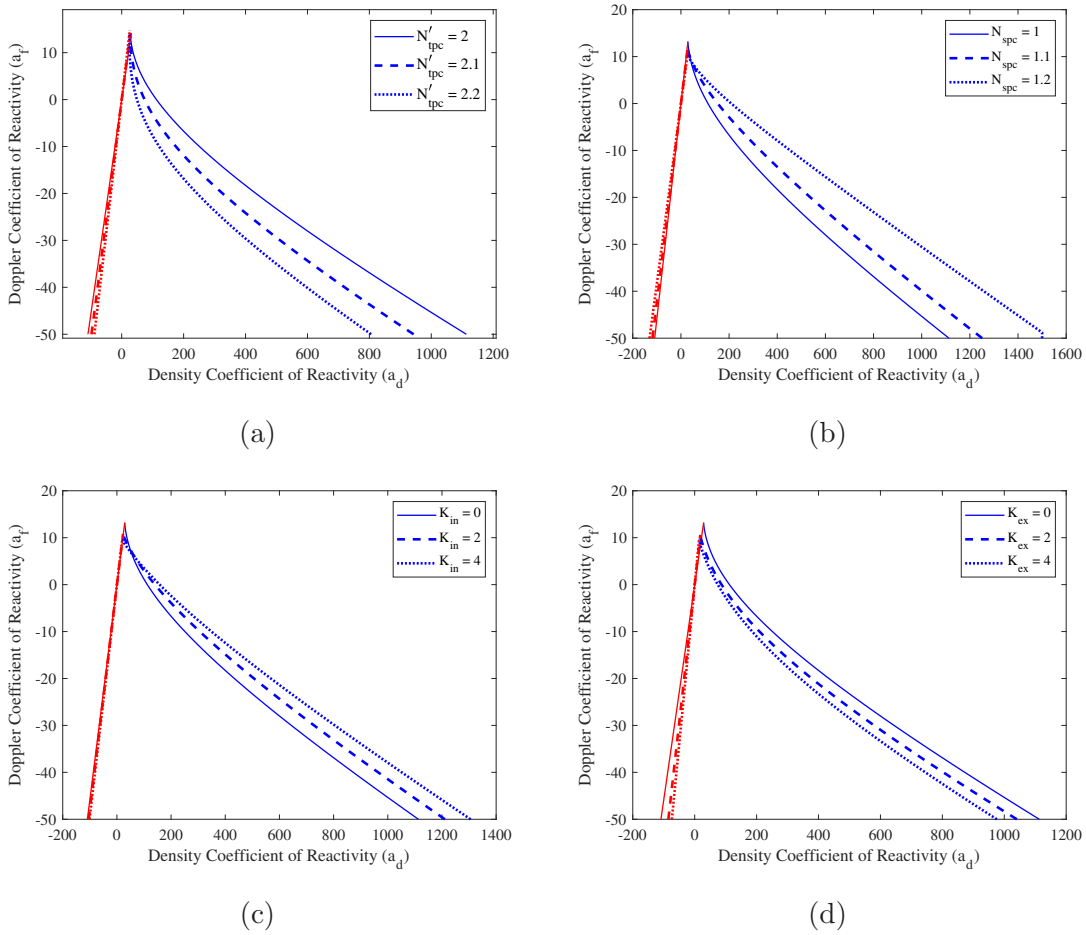

Figure 5: Effect of various parameters on stable region of SCLWR with $F_r = 0.03$, $N_f = 4.34$ (a) for different N'_{tpc} ($N_{spc} = 1$, $K_{in} = 0$, $K_{exit} = 0$) (b) for different N_{spc} ($N'_{tpc} = 2$, $K_{in} = 0$, $K_{exit} = 0$) (c) for different K_{in} ($N'_{tpc} = 2$, $N_{spc} = 1$, $K_{exit} = 0$) and (d) for different K_{exit} ($N'_{tpc} = 2$, $N_{spc} = 1$, $K_{in} = 0$)

5.1. Effects on $a_d - a_f$ plane

From Fig. 5, a few observations have been made as follows:

1. Increase in heat flux (N'_{tpc}) shrinks the stable operation region in $a_d - a_f$ plane (Fig. 5a). This indicates that, an increase in heat flux produce de-stabilizing effect to the system operation. This is due to the fact that, an increase in heat flux decreases the average density of the fluid inside the flow channel. Hence, for the same amount of Doppler reactivity, the density coefficient of reactivity must be lowered down to maintain a constant total reactivity (Eq. 3) of the reactor core for stable operation.
2. Increase in pseudo-subcooling (N_{spc}) shrinks the stable operation region in $a_d - a_f$ plane (Fig. 5b). This indicates that, an increase in pseudo-subcooling produce de-stabilizing effect to the system operation. This is due to the fact that, an increase in pseudo-subcooling also decreases the average density of the fluid inside the flow channel. Hence, for the same amount of Doppler reactivity, the density coefficient of reactivity must be lowered down to maintain a constant total reactivity (Eq. 3) of the reactor core for stable operation.
3. Increase in inlet pressure loss coefficient (K_{in}) broadens the stable operation region in $a_d - a_f$ plane (Fig. 5c). This indicates that, an increase in inlet pressure loss coefficient (K_{in}) produce stabilizing effect to the system operation. This is because, the inlet pressure loss coefficient (K_{in}) resists the inlet flow and acts as a damping agent to the oscillations.
4. Compared to K_{in}, an opposite effect (de-stabilizing effect) is shown (Fig. 5d) by exit pressure loss coefficient (K_{exit}). An increase in exit pressure loss coefficient (K_{exit}) shrinks the stable operation region in $a_d - a_f$ plane . This is because, the exit loss coefficient acts as a suction for the flow which in-turn drive the oscillations.

5.2. Effects on $N'_{tpc} - N_{spc}$ plane

From Fig. 6, a few observations have been made as follows:

1. Increase in K_{in} produces similar stabilizing effect (Fig. 6a) as shown in Fig. 5c.
2. Increase in K_{exit} produces similar de-stabilizing effect (Fig. 6b) as shown in Fig. 5d.
3. Increase in Doppler coefficient of reactivity shrinks the stable region (Fig. 6c) and hence produces de-stabilizing effect. This is because, when the Doppler coefficient of

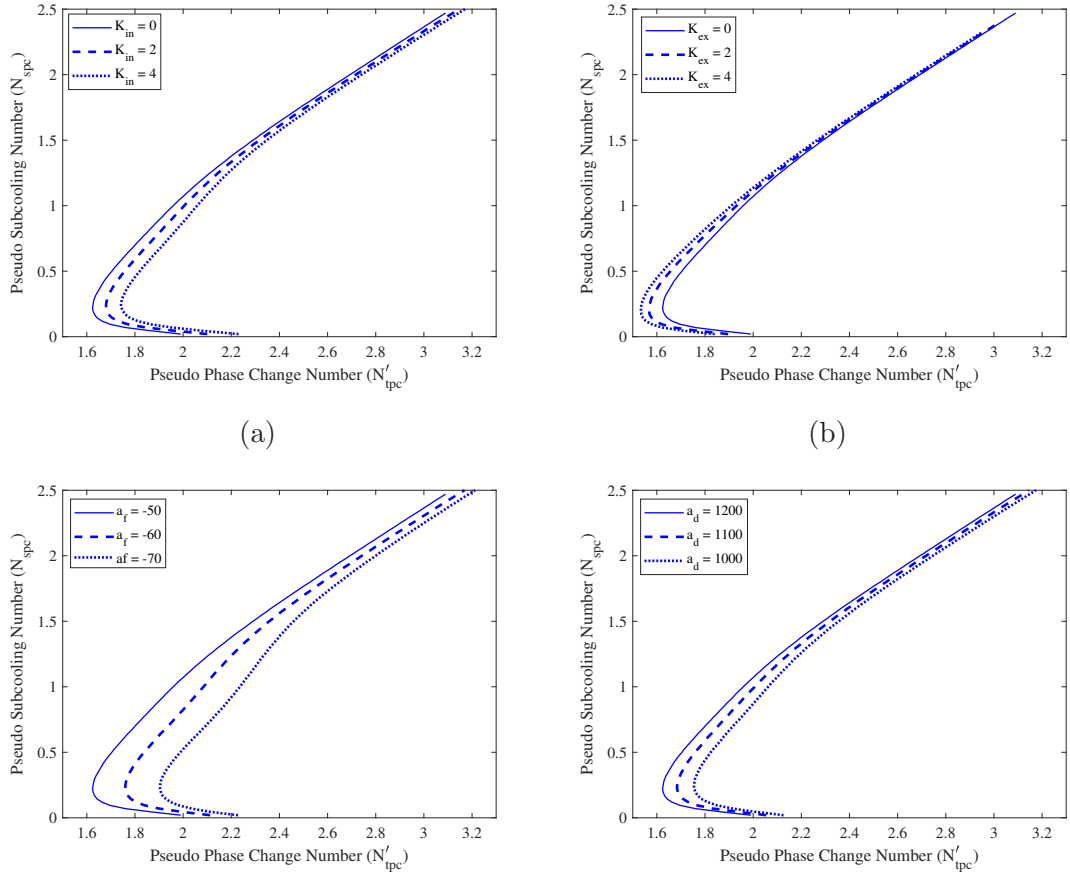

Figure 6: Effect of various parameters on stable region of SCLWR with $F_r = 0.03$, $N_f = 4.34$ (a) for different K_{in} ($a_f = -50$, $a_d = 1200$, $K_{exit} = 0$) (b) for different K_{exit} ($a_f = -50$, $a_d = 1200$, $K_{in} = 0$) (c) for different a_f ($\alpha_d = 1200$, $K_{in} = 0$, $K_{exit} = 0$) and (d) for different a_d ($a_f = -50$, $K_{in} = 0$, $K_{exit} = 0$)

reactivity is increased, it increases the total reactivity and hence power of the reactor. At the same pseudo-subcooling, when power of the reactor increases, it lowers the exit density of the fluid and increases the pressure drop (suction) across the flow channel. This increased suction acts as a driving force to the oscillations.

4. Similar de-stabilizing effect is observed for density coefficient of reactivity (Fig. 6d). When density coefficient of reactivity is increased, it increases the total reactivity and power of the reactor and hence pressure drop across the channel, which then acts as a driving force to the oscillations.

6. Nonlinear Stability Analysis (Second Level)

6.1. Step 1: Identify the Type of Hopf Bifurcation

The second level for analyzing the instabilities is to identify the type of Hopf bifurcations. In general, there are two types of Hopf bifurcations namely, 1. Supercritical Hopf and 2. Subcritical Hopf. The detailed explanations of the characteristics of these Hopf bifurcations can be found in Paul and Singh (2017b). To identify the occurrence of these Hopf bifurcations, the First Lyapunov Coefficients (FLCs, (Paul and Singh, 2017b)) along the linear stability boundaries are calculated. For a supercritical Hopf (subcritical Hopf), the FLCs are negative (positive). The variations of the FLCs along the stability boundaries are plotted in Fig. 7. It should be noted that, the phenomenon of separation between supercritical and subcritical Hopf bifurcation is known as Generalized Hopf bifurcation, and the corresponding point is called as the Generalized Hopf (GH) point. At the GH point the FLC becomes zero.

It is seen from Fig. 7 that, the FLC changes it′s sign once along the stability boundary in the $N'_{tpc} - N_{spc}$ plane, however, the FLC changes it's sign twice in $a_d - a_f$ plane. This implies that along-with the thermal-hydraulic parameters ($N'_{tpc} - N_{spc}$) the reactivities of the SCLWR play dominant role in defining the nonlinear stability behavior of the system.

6.2. Step 2: Understanding of the Limit Cycles

A Hopf bifurcation is always accompanied by the existence of limit cycles at the vicinity of the bifurcation boundary. There are two types of limit cycles namely 1. stable limit cycles and 2. unstable limit cycles. The stable limit cycles (unstable limit cycles) are closed trajectories which attract (repel) the nearby trajectories. The detailed discussion of the limit cycles can be found in Strogatz (1994). In the supercritical Hopf bifurcation region, small amplitude stable limit cycles are found in unstable side of the stability boundary. In the subcritical Hopf bifurcation region, small amplitude unstable limit cycles are found in the stable side of the stability boundary. However, these small amplitude unstable limit cycles are again encircled by stable limit cycles.

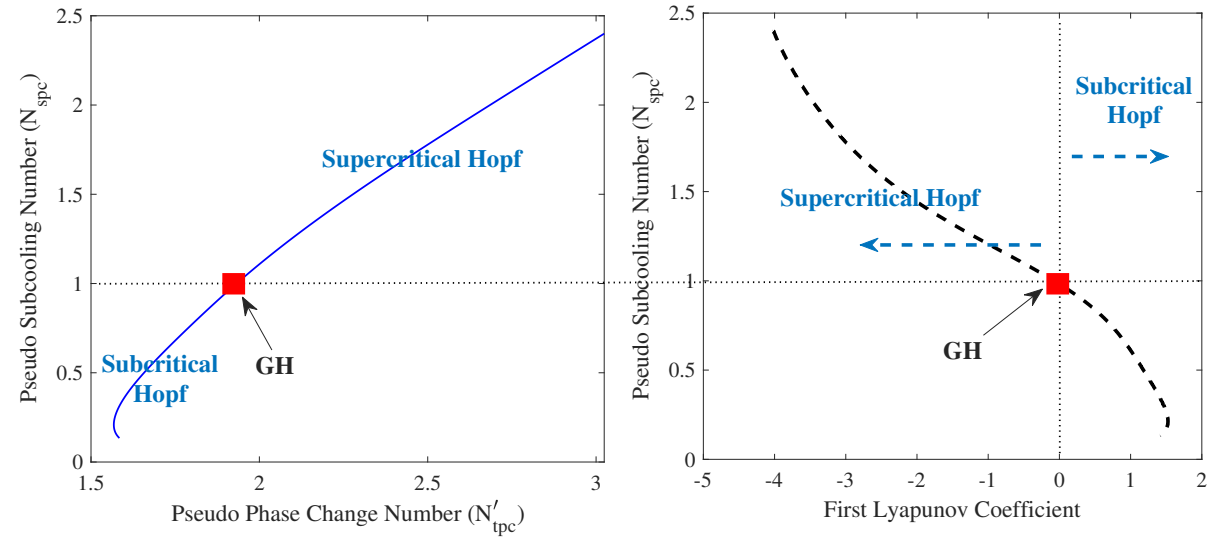

(a)

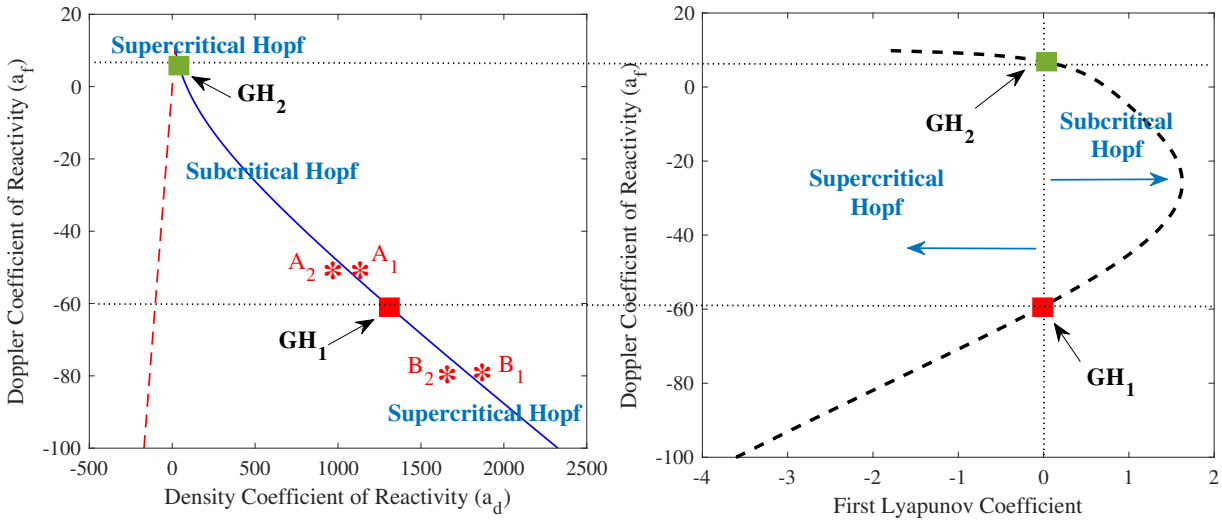

(b)

Figure 7: (a) **Left:** Stability boundary in $N'_{tpc}-N_{spc}$ plane and **Right:** Variation of FLCs along the stability boundary showing occurrence of sub- and supercritical Hopf bifurcation (b) **Left:** Stability boundary in $a_d - a_f$ plane and **Right:** Variation of FLCs along the stability boundary showing occurrence of two subcritical and one supercritical Hopf bifurcation regions

The above-said characteristics of the limit cycles and sub- & supercritical Hopf bifurcations are confirmed by the numerical simulations carried out at various points (Table 2) of the stability map (Fig. 7).

Table 2: Points considered to verify oscillation characteristics

Fig. no	a_d	a_f	Amount of perturbation (% of P_0)
7a	1045	-50	0.1
7b	1045	-50	2000
7c	1038	-50	1
7d	1038	-50	70
7e	1038	-50	2000
8a	1805	-80	0.1
8b	1805	-80	80
8c	1795	-80	10
8d	1795	-80	400

For the numerical simulations, the system of ODEs (Eq. 55 to Eq. 62) are solved numerically using ODE45 solver in MATLAB. The point A_1 being on the unstable side shows growing oscillations (Fig. 8a) for small perturbation. However, due to the existence of the stable limit cycle in this region, the growing oscillations (decaying oscillations, for large perturbation) settle down (Fig. 8a and Fig. 8b) around the stable limit cycle. The point A_2 being in the stable side of the stability boundary shows decaying oscillations (Fig. 8c) with small perturbation. However, when large perturbation is applied, the oscillations grow (Fig. 8d) due to the existence of unstable limit cycle in this region. These growing oscillations (decaying oscillations, even larger perturbation) again settle down (Fig. 8d and Fig. 8e) around a stable limit cycle. These phenomena confirms the occurrence of the subcritical Hopf bifurcation at the vicinity of the stability boundary.

The point B_1 being on the unstable side shows growing oscillations (Fig. 9a) for small perturbation. However, due to the existence of the stable limit cycles in this region, the growing (decaying for large perturbation) oscillations settle down (Fig. 9a and Fig. 9b) around the stable limit cycle. The point B_2 being in the stable side of the stability boundary shows decaying oscillations for both small (Fig. 9c) and large (Fig. 9d) perturbations. These phenomena confirms the occurrence of the supercritical Hopf bifurcation at the vicinity of

the stability boundary.

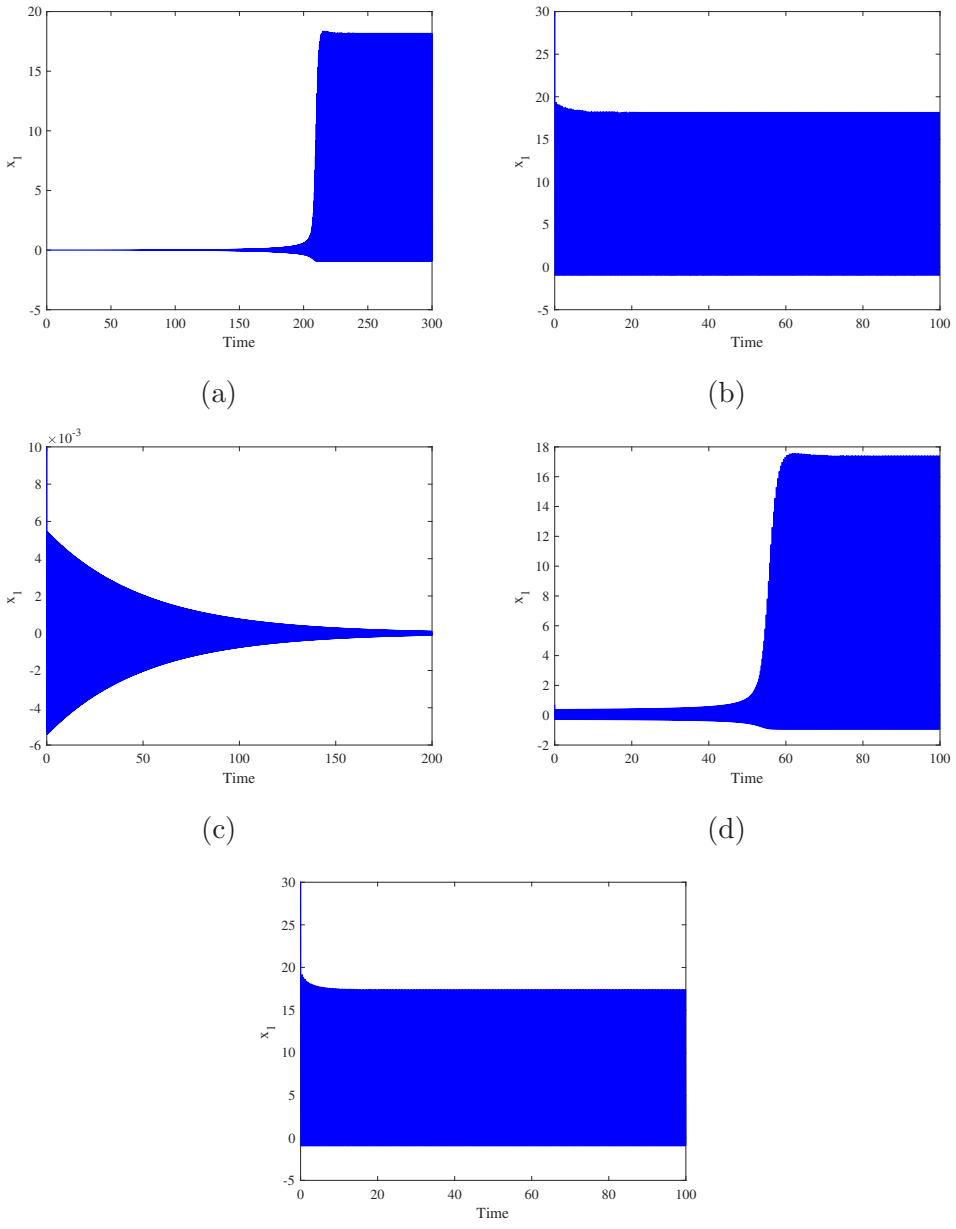

Figure 8: Case of subcritical Hopf bifurcation (a) Point A_1: Growing oscillations with small perturbation settle into a stable limit cycle (b) Point A_1: Decaying oscillations with large perturbation settle into a stable limit cycle (c) Point A_2: Decaying oscillations with small perturbation (d) Point A_2: Growing oscillations with large perturbation settle into a stable limit cycle (e) Point A_2: Decaying oscillations with even larger perturbation settle into a stable limit cycle

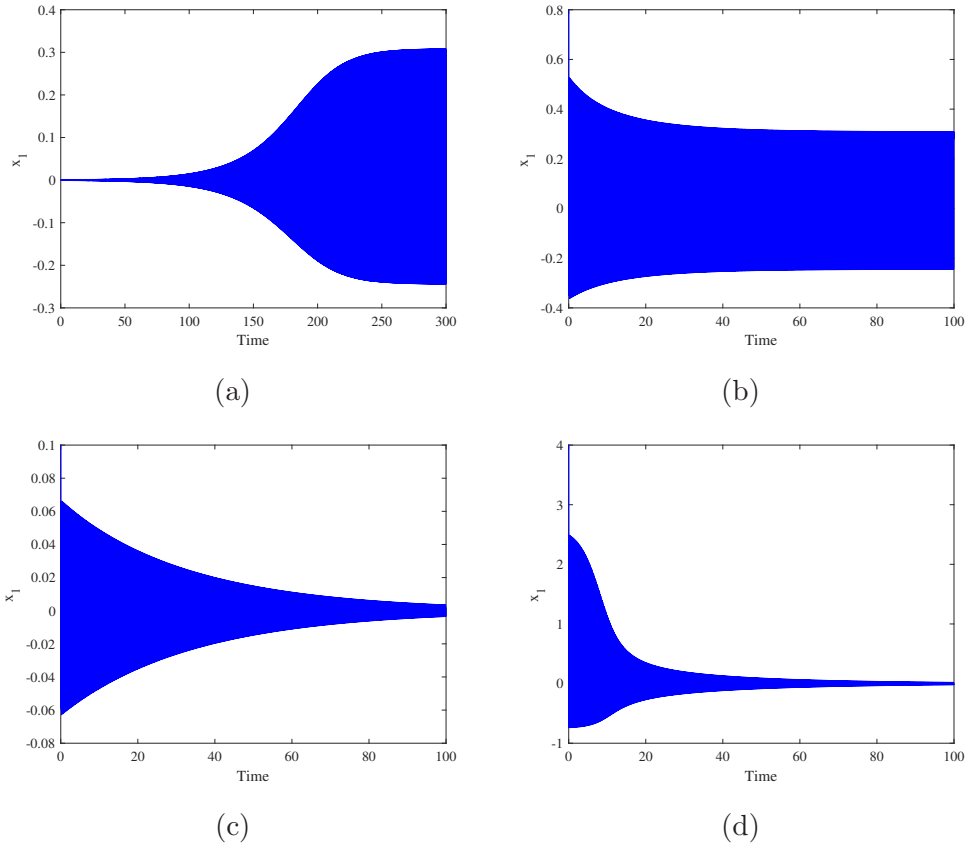

Figure 9: Case of supercritical Hopf bifurcation (a) Point B_1: Growing oscillations with small perturbation settle into a stable limit cycle (b) Point B_1: Decaying oscillations with large perturbation settle into a stable limit cycle (c) Point B_2: Decaying oscillations with small perturbation (d) Point B_2: Decaying oscillations with large perturbation

6.3. Step 3: Saddle Node Bifurcation and a Turning Point

The saddle node bifurcation or fold bifurcation is a co-dimension one bifurcation. In this bifurcation, two limit cycles (stable and unstable) of a dynamical system collide and disappear. In the stable side of the subcritical Hopf bifurcation region, if we start varying one parameter of the system from the Hopf point, a saddle node bifurcation appears when one of the eigenvalues of the monodromy matrix (or Floquet multipliers) becomes one. In the present analysis, the Floquet multipliers of the system are calculated using the MATCONT bifurcation package. The corresponding location in the parameter space where this bifurcation appears is called as a turning point or a limit point of cycles (LPC). A gen-

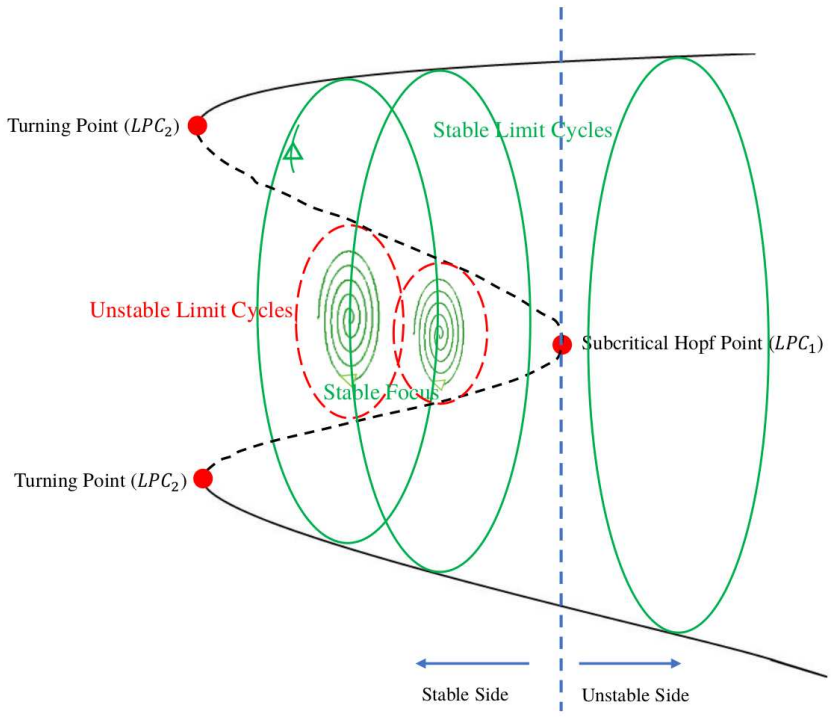

Figure 10: Generalized view of a turning point

eralized view of a turning point is shown in Fig. 10. In the subcritical Hopf bifurcation region, a small amplitude unstable limit cycle appear at the Hopf point (LPC_1), which is surrounded by a large amplitude stable limit cycle. As we go deep into the stable side by varying only one system parameter, the amplitudes of the unstable limit cycles corresponding to each location on the parameter space keep on increasing. Moreover, the amplitudes of the stable limit cycles that surround these unstable limit cycles keep on decreasing. At the turning point represented by LPC_2, the amplitudes of both unstable and stable limit cycles become equal and thus at this point both these limit cycles collide and disappear. It can also be seen that the stable limit cycles continue to appear even on the unstable side of the stability boundary. Thus, the oscillations will never grow for infinite time and will settle into constant large amplitude stable limit cycles even when the system is operated under unstable operating conditions. In the present study one such turning point is shown in Fig. 11. It is seen that, the numerical simulations shown in the Fig. 8 are in agreement with that

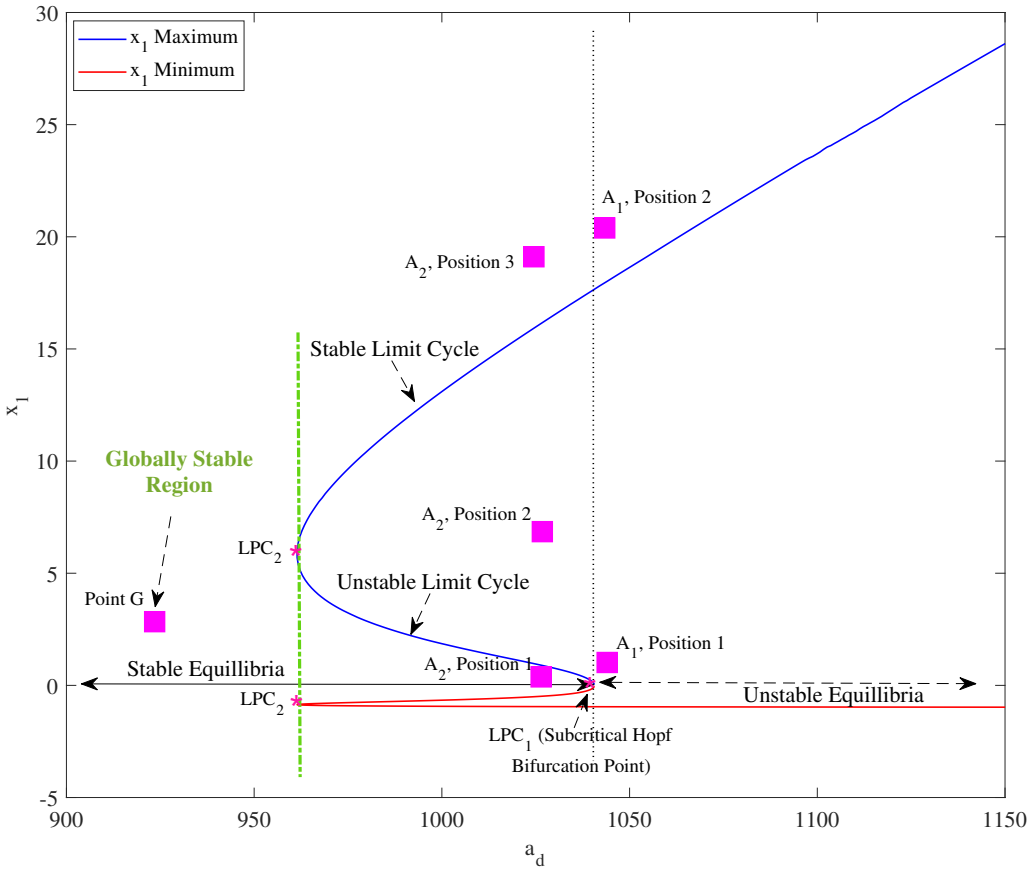

Figure 11: View of an actual saddle node bifurcation and a turning point. The point LPC_2 represents the turning point. The region left to the LPC_2 is the globally stable region. The region between LPC_2 & LPC_1 is the bistable region.

expected according to their positions in the Fig. 11. When small (position 1) and large (position 2) perturbations are applied at the point A_1 , the trajectories move towards the large amplitude stable limit cycle, and hence growing & decaying oscillations are observed. At point A_2, when small perturbation is applied (position 1), the trajectories move away from the unstable limit cycle and hence decaying oscillations are observed. However, when large perturbation is applied at point A_2 (position 2), the trajectories again move away from the unstable limit cycle and settle around the large amplitude stable limit cycle. Furthermore, at point A_2; by applying even more perturbation (position 3), the stable limit cycle attracts the trajectories and hence decaying oscillations are observed. It is also noted that, in the

subcritical Hopf bifurcation region, the Hopf points are always represented as the first limit point of cycles (LPC_1), however, they do not represent the turning points.

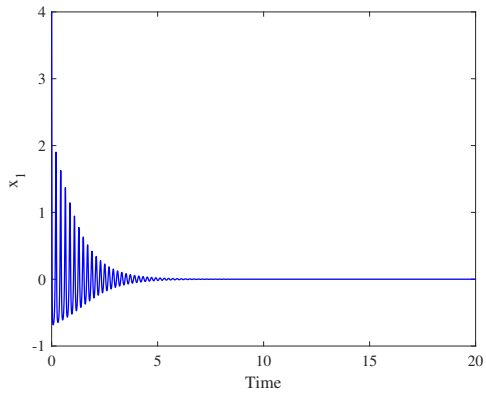

(a) Perturbation: 400% of P_0

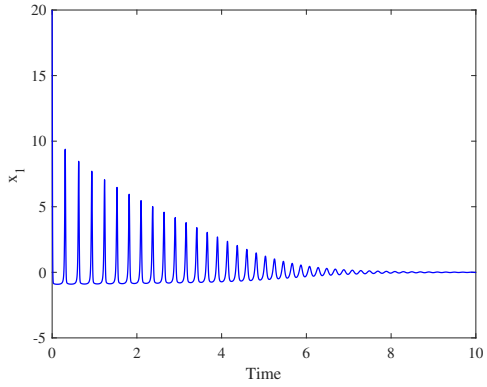

(b) Perturbation: 2000% of P_0

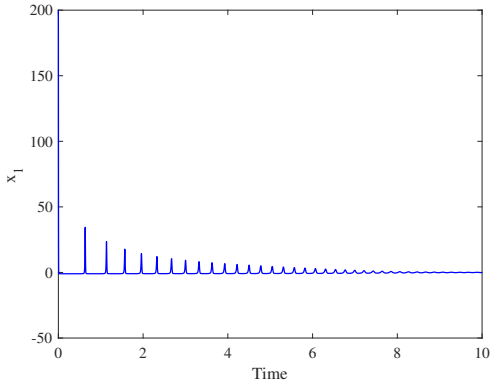

(c) Perturbation: 20000% of P_0

Figure 12: Oscillations at point G, showing globally stable behavior for very large perturbation

6.4. Step 4: Identification of the Globally Stable Region

It is worth noting that, the left hand side of the green vertical dashed line in the Fig. 11 do not contain any limit cycle. Hence, this region is said to be globally stable. To confirm this phenomenon, numerical simulations for very large perturbations are done at point G shown in Fig. 12. Decaying oscillations are observed for very large perturbation, hence this region is confirmed as globally stable. Moreover, the region between LPC_1 and LPC_2 is known as the Bistable region. This is because, this region shows dual characteristics of

both stable and unstable limit cycles which depend on the amount of perturbation in the system. The loci of all the turning points (LPC_2) in Fig. 13a and Fig. 13b are known as the nonlinear stability boundaries (also known as the limit point of cycles curves).

Conclusions

In this work, the development of a simplified SCLWR nuclear coupled thermal hydraulic reduced order model is presented. The model couples 1-D reduced-order thermal hydraulics, point kinetics with one group of delayed neutrons and fuel heat transfer phenomena inside the reactor core. Only two intrinsic reactivity feedbacks, namely, Doppler reactivity feedback and density reactivity feedback are considered to study the SCLWR dynamics. The system stability has been studied in two different sets of parameter spaces: (1) the thermal hydraulic parameters ($N'_{tpc} - N_{spc}$) and (2) the intrinsic reactivity feedbacks ($a_d - a_f$). Following conclusions are made with this study:

1. Increase in inlet pseudo-subcooling widens the stable operation region both on thermal-hydraulic parameter plane and reactivity feedback plane. This indicates, an increase in inlet pseudo-subcooling will stabilize the system.
2. Increase in Doppler reactivity will drive the system towards unstable operating conditions.
3. An increase in heat flux has destabilizing effect to the system on reactivity feedback plane.
4. An increase in inlet pressure loss coefficient will stabilize the system.
5. Compared to inlet pressure loss coefficient, an increase in exit pressure loss coefficient will destabilize the system.

Moreover, the model shows the occurrence of two types of Hopf bifurcation (subcritical and supercritical). In addition it shows the existence of turning points in the stable side of the linear stability boundary which also denote the threshold of nonlinear stability.

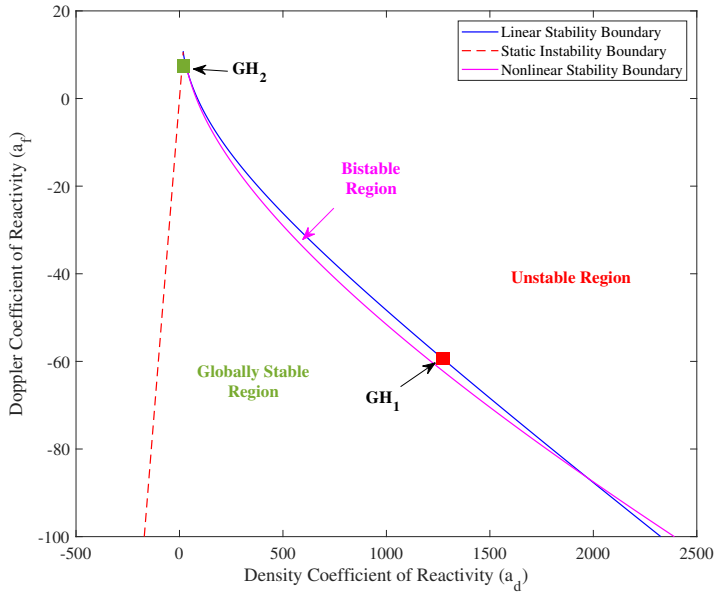

(a)

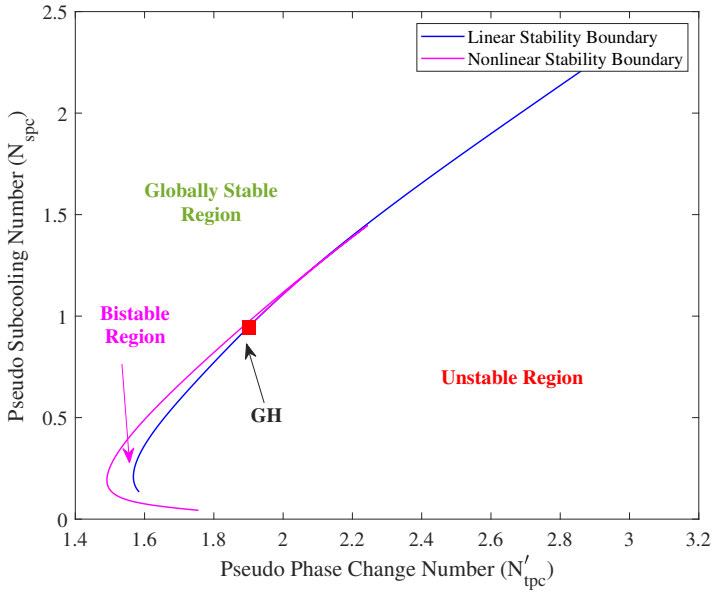

(b)

Figure 13: Nonlinear stability boundaries showing the bistable region and globally stable region on (a) a_d-a_f plane, and (b) N'_{tpc}-N_{spc} plane

Nomenclature

A_C^*	Cross sectional area of the coolant channel (m^2)
C_q^*	Heat generated in the SCLWR channel (W)
C_{pc}^*	Specific heat of the coolant at pseudo-critical temperature ($J\,kg^{-1}\,K^{-1}$)
C_{PF}^*	Specific heat of the fuel rod ($J\,kg^{-1}\,K^{-1}$)
D_e^*	Equivalent diamater of the fuel rod (m)
D_h^*	Hydraulic diamater of the flow channel (m)
f	Friction factor
G^*	Mass flux ($kg\,m^{-2}\,s^{-1}$)
g^*	Acceleration due to gravity ($m\,s^{-2}$)
H^*	Heat transfer coefficient ($W\,m^{-2}\,K^{-1}$)
k^*	Thermal conductivity of the fuel rod ($W\,m^{-1}\,K^{-1}$)
K_{exit}	Exit pressure loss coefficient
K_{in}	Inlet pressure loss coefficient
L_{ch}^*	Length of the flow channel (m)
N_f	Friction number
N_{spc}	Pseudo subcooling number
N_{tpc}	Pseudo phase change number
Nu	Nusselt number
P_h^*	Peremeter of coolant channel (m)

Pr Prandtl number

q''^* Wall heat flux ($\mathrm{W\,m^{-2}}$)

q'''^* Heat generation rate per unit volume ($\mathrm{W\,m^{-3}}$)

R_D^* Doppler reactivity (dk/k)

R_d^* Density reactivity (dk/k)

Re Reynold's number

T_{F0}^* Steady-state fuel rod temperature (K)

T_F^* Fuel rod temperature (K)

T_{in}^* Coolant inlet temperature (K)

T_{pc}^* Pseudo-critical temperature (K)

w^* Velocity of the coolant ($\mathrm{m\,s^{-1}}$)

w_0^* Inlet velocity of the coolant ($\mathrm{m\,s^{-1}}$)

C^* Average delayed neutron precursor density ($\mathrm{m^{-1}}$)

h^* Specific enthalpy of coolant $\mathrm{J\,kg^{-1}}$

h_{in}^* Inlet specific enthalpy of coolant $\mathrm{J\,kg^{-1}}$

h_{pc}^* Specific enthalpy at pseudo-critical temperature $\mathrm{J\,kg^{-1}}$

h_{pc}^* Specific enthalpy of coolant at pseudo-critical temperature $\mathrm{J\,kg^{-1}}$

N^* Average neutron density inside the reactor ($\mathrm{m^{-3}}$)

R^* Reactivity (dk/k)

Greek Letters

α_d^* Density coefficient of reactivity ($dk/k \quad \mathrm{m^3\,kg^{-1}}$)

α_f^* Fuel tempearature coefficient of reactivity (dk/k K^{-1})

β_{pc}^* Isobaric thermal expansion coefficient (K^{-1})

ΔP^* Pressure drop (Pa)

ρ^* Density of the coolant ($\mathrm{kg\,m}^{-3}$)

ρ_{avg0}^* Steady-state average density of the coolant ($\mathrm{kg\,m}^{-3}$)

ρ_{avg}^* Average density of the coolant ($\mathrm{kg\,m}^{-3}$)

ρ_F^* Density of the fuel rod ($\mathrm{kg\,m}^{-3}$)

ρ_{pc}^* Density at pseudo-critical temperature ($\mathrm{kg\,m}^{-3}$)

β Delayed neutron fraction

Λ^* Neutron generation time (s)

λ^* Decay constant for delayed neutron precursors (s^{-1})

ν^* Specific volume of the coolant $\mathrm{m}^3\,\mathrm{kg}^{-1}$

τ^* Time (s)

Appendix A.

The non-dimensional parameters used to develop the present model are as follows:

$$x_1 = \frac{N^* - N_0^*}{N_0^*} = \frac{P^* - P_0^*}{P_0^*} \qquad x_2 = \frac{C^* - C_0^*}{C_0^*} \qquad x_3 = \frac{T_F^* - T_{F0}^*}{T_{F0}^*}$$

$$\xi_1 = \frac{P_h^* H^* L_{ch}^* (T_{F0}^* - T_{pc}^*)}{A_c^* \rho_F^* C_{PF}^* T_{F0}^* w_0^*} \qquad \xi_2 = \frac{P_h^* H^* L_{ch}^*}{A_c^* \rho_F^* C_{PF}^* w_0^*} \qquad N_{tpc} = \frac{H^* T_{F0}^* P_h^* \beta_{pc}^* L_{ch}^*}{A_c^* \rho_{pc}^* C_{pc}^* w_0^*}$$

$$N_{spc} = \frac{\beta_{pc}^*}{C_{pc}^*}(h_{pc}^* - h_{in}^*) \qquad h = \frac{\beta_{pc}^*}{C_{pc}^*}(h^* - h_{pc}^*) \qquad N_f = \frac{f L_{ch}^*}{2 D_h^*}$$

$$a_f = \frac{\alpha_f^* T_{F0}^*}{\beta} \qquad a_d = \frac{\alpha_d^* \rho_{pc}^*}{\beta} \qquad \rho = \frac{\rho^*}{\rho_{pc}^*}$$

$$\lambda = \frac{\lambda^* L_{ch}^*}{w_0^*} \qquad \Lambda = \frac{\beta L_{ch}^*}{\Lambda^* w_0^*} \qquad \Delta = \frac{T_{pc}^*}{T_{F0}^*}$$

$$A_1 = \frac{\rho_{in} - \rho_{pc}}{(h_{pc} - h_{in})\rho_{in}\rho_{pc}} \qquad A_2 = \frac{\rho_{pc} - \rho_{exit}}{(h_{exit} - h_{pc})\rho_{pc}\rho_{exit}} \qquad \Delta P = \frac{\Delta P^*}{\rho_{pc}^* w_0^{2*}}$$

$$w = \frac{w^*}{w_0^*} \qquad z = \frac{z^*}{L_{ch}^*} \qquad t = \frac{\tau^*}{L_{ch}^*/w_0^*}$$

Appendix B.

Appendix B.1. Justification for enthalpy approximation

The approximation for the enthalpy (Eq. 21) is made in analogy to that made for subcritical water flow systems (Paul and Singh, 2014b,a, 2015) This type of approximation was first proposed by Clausse and Lahey (1991). Using constant heat flux assumption, Clausse and Lahey (1991) proposed a model for density wave oscillations for two-phase flow systems by dividing the single-phase region into N number of equidistant nodes, and the enthalpy was approximated between consecutive nodes as,

$$h_n = h_{in} + \frac{n-1}{N-1}(h_{sat} - hin) \tag{B.1}$$

where it was also stated that, though h_n is a constant but its spatial location is time dependent. Now, the enthalpy h(z,t) at any location z was written as,

$$h(z,t) = h_{in} + \frac{z}{\mu(t)}(h_{sat} - hin) \tag{B.2}$$

Hence, this form of approximation is also used in the case of supercritical fluids shown by Eq. 21. Note that, the term excluding the z in R.H.S of Eq. B.2 is denoted as $a_1(t)$ in Eq. 21.

Appendix B.2. Justification for density approximation

To understand the approximation for the density, let us first observe the variation of specific volume of a supercritical fluid with temperature, which is shown by Fig. B.14.

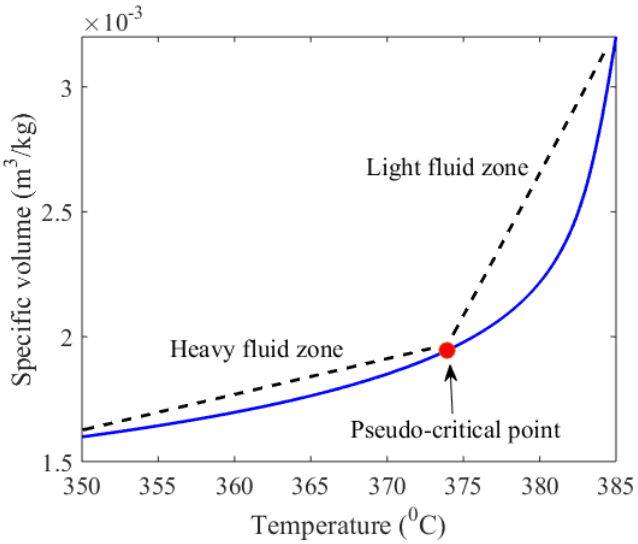

Figure B.14: Variation of specific-volume with temperature of a supercritical fluid

To approximate the density in the above-shown two zones, it is first assumed that, at steady-state; when the temperature of the fluid increases linearly along the length of the channel, the specific volume of the fluid also increases linearly with temperature as shown by the dashed lines in Fig. B.14.

Hence, at steady-state; the variation of specific enthalpy along the length of the flow channel can be written as:

$$\upsilon(z) = \upsilon_{in} + \Gamma * z \tag{B.3}$$

where Γ is the proportionality constant which relates the specific-volume and the channel location z and is given by Eq. 46. Similarly, during transient operation of the system, the

specific volume is assumed to be a linear function of channel position, and thus it can be written as:

$$\upsilon(z,t) = \upsilon_{in} + \Gamma(t) * z \tag{B.4}$$

It should be noted that, now the proportionality constant becomes a function of time ($\Gamma(t) = b_1(t)$) to represent the time dependency of the specific-volume.
By simplifying the Eq. B.4 we get:

$$\rho(z,t) = \frac{1}{\frac{1}{\rho_{in}} + b_1(t) * z} \tag{B.5}$$

Appendix B.3. Justification for velocity approximation

In case of a two-phase flow system with subcritical fluid, the mixture velocity is given by Verma et al. (2018):

$$\frac{\partial w_m^*}{\partial z^*} = \frac{q^{"*} P_h^* \Delta\rho^*}{\rho_f^* \rho_g^* A_c^* \Delta h_{fg}^*} \tag{B.6}$$

After non-dimensionalizing suitably and by further simplification, the above equation can be written as:

$$w_m(z,t) = w_{in}(t) + N_{pch} z \tag{B.7}$$

In analogy to the Eq. B.7, in case of a supercritical fluid, the velocity is approximated as:

$$w(z,t) = w_{in}(t) + A_1 N_{tpc}(1-\Delta) z \tag{B.8}$$

Note that, there is no direct theoretical relation present for a supercritical fluid which can correlate the fluid velocity with heat flux as done in case of a subcritical fluid (Eq. B.6). However, to find the relation equation of continuity at steady-state with incompressible flow assumption ($\frac{\partial(\rho w)}{\partial z} = 0$) is used. Since the density variation of the fluid with position is known (Eq. B.4), hence after simplifying $\frac{\partial(\rho w)}{\partial z} = 0$ we get the above relation for fluid velocity (Eq. B.8).

Appendix C.

Appendix C.1. Hopf bifurcation

A qualitative change in the behavior of a dynamical system by varying a parameters of the system is known as a bifurcation. The Poincare–Andronov–Hopf (PAH) bifurcation, dominantly known as the Hopf bifurcation is a special type of bifurcation which appears in a nonlinear dynamical system when certain conditions are met (Strogatz, 1994). This bifurcation guarantees the existence of periodic (stable and unstable) solutions. Moreover, it is known as co-dimension one bifurcation (a bifurcation which is observed by varying only one free parameter at a time) and is also referred as local bifurcation. Recently this bifurcation is widely studied for Boiling Water Reactors (BWRs) (Rizwan-uddin, 2006; Bindra and Rizwan-uddin, 2014; Wahi and Kumawat, 2011).

The conditions for Hopf bifurcation to occur are as follows:

1. The minimum number of dimensions of the system must be two.
2. The system must possess at-least one pair of complex conjugate eigenvalues.
3. At the critical parameter (λ_c, the parameter defining the linear stability threshold) the eigenvalues must be purely imaginary ($\pm\iota\omega$).

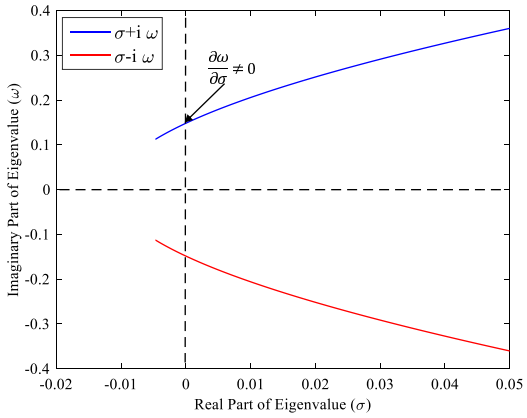

Figure C.15: Variation of eigenvalues around the critical point

4. If the real (σ) and imaginary parts (ω) of the eigenvalues are plotted on a complex plane along X- & Y- axes respectively, the loci of all the plotted eigenvalues as the system parameter (λ) is varied from stable to unstable side of the linear stability boundary, must cross the imaginary axis at non-zero rate as shown in Fig C.15.

Appendix C.2. Static instability

It should be noted that, in Hopf bifurcation, we observe growing oscillations in the unstable side when small perturbation is applied to the system. However, in static instability region, no oscillations are observed and the system suddenly jumps from one operating condition to another (Fig. C.16). The threshold of the static instability region is known as branch point (BP) where one real eigenvalue of the system becomes zero.

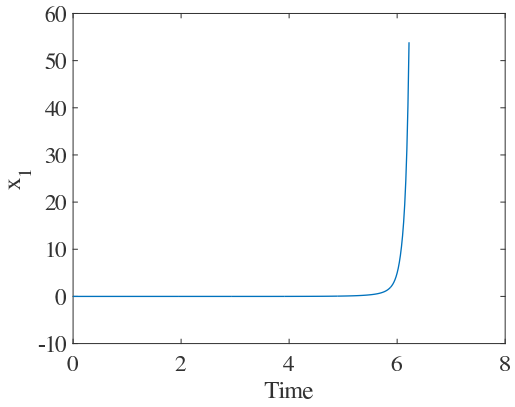

Figure C.16: No oscillations are observed in static instability region

Appendix D.

All the functions defined earlier to develop the model are given in this section.

$$M_{tpc} = N_{tpc} \times [x_3 + 1 - \Delta]$$

$$\Phi_1(t) = \frac{-(a_1A_1 - b_1)b_1(L_1 - L_{in})M_{tpc}\rho_{in} + a_1(A_1M_{tpc} + b_1\rho_{in}(dL_{in} - v_{in}))Log[1 + b_1(L_1 - L_{in})\rho_{in}]}{b_1(L_1 - L_{in})\rho_{in} - Log[1 + b_1(L_1 - L_{in})\rho_{in}]} \tag{D.1}$$

$$\Phi_2(t) = -\Bigg[\frac{\rho_{in}v_{in} - \rho_1(A_1(L_1 - L_{in})M_{tpc} + v_{in}))}{b_1(-L_1 + L_{in})\rho_{in} + (1 + b_1(L_1 - L_{in})\rho_{in})Log[1 + b_1(L_1 - L_{in})\rho_{in}]}$$
$$+ \frac{-(((L_1 - L_{in})(d\rho_{in} + b_1 dL_{in}\rho_{in}^2))/(1 + b_1(L_1 - L_{in})\rho_{in}))}{b_1(-L_1 + L_{in})\rho_{in} + (1 + b_1(L_1 - L_{in})\rho_{in})Log[1 + b_1(L_1 - L_{in})\rho_{in}]}\Bigg]$$
$$\times (b_1^2(1 + b_1(L_1 - L_{in})\rho_{in}) \quad \text{(D.2)}$$

$$\Phi_3(t) = \frac{M_{tpc}b_2^2(L_1 - L_2)\rho_1 - a_2(A_2 M_{tpc}Log(1 + b_2(L_2 - L_1)\rho_1)}{Log(1 + b_2(L_2 - L_1)\rho_1) + b_2(L_1 - L_2)\rho_1}$$
$$+ \frac{b_2\rho_1(A_2 M_{tpc}(L_1 - L_2) + Log(1 + b_2(L_2 - L_1)\rho_1)(-v_1 + dL_1)))}{Log(1 + b_2(L_2 - L_1)\rho_1) + b_2(L_1 - L_2)\rho_1} \quad \text{(D.3)}$$

$$\Phi_4(t) = \frac{b_2^2(-1 + b_2(L_1 - L_2)\rho_1)(\rho_1 v_1 - \rho_2(A_2 M_{tpc}(L_2 - L_1) + v_1)}{Log(1 + b_2(L_2 - L_1)\rho_1) - b_2(L_1 - L_2)(-1 + Log(1 + b_2(L_2 - L_1)\rho_1))\rho_1}$$
$$+ \frac{-((L_1 - L_2)(b_2\rho_1^2 dL_1 + d\rho_1))/(-1 + b_2(L_1 - L_2)\rho_1))}{Log(1 + b_2(L_2 - L_1)\rho_1) - b_2(L_1 - L_2)(-1 + Log(1 + b_2(L_2 - L_1)\rho_1))\rho_1} \quad \text{(D.4)}$$

$$\Delta P_1 = -((A_1 M_{tpc}Log(1 + b_1(L_1 - L_{in})\rho_{in})dL_{in})/b_1)$$

$$\Delta P_2 = (Log(1 + b_1(L_1 - L_{in})\rho_{in}))/b_1$$

$$\Delta P_3 = (A_1 M_{tpc}(-A_1 M_{tpc}Log(1 + b_1(L_1 - L_{in})\rho_{in}) + b_1\rho_{in}(A_1 M_{tpc}(L_1 - L_{in})$$
$$+ Log(1 + b_1(L_1 - L_{in})\rho_{in})v_{in})))/(b_1^2\rho_{in})$$

$$\Delta P_4 = N_f \times \Bigg[(1/(2b_1^3\rho_{in}^2))(2A_1^2 M_{tpc}^2 Log(1 + b_1(L_1 - L_{in})\rho_{in})$$
$$+ b_1\rho_{in}(A_1^2 M_{tpc}^2(L_1 - L_{in})(-2 + b_1(L_1 - L_{in})\rho_{in})$$
$$- 4A_1 M_{tpc}(Log(1 + b_1(L_1 - L_{in})\rho_{in}) + b_1(-L_1 + L_{in})\rho_{in})v_{in}$$
$$+ 2b_1 Log(1 + b_1(L_1 - L_{in})\rho_{in})\rho_{in}v_{in}^2))\Bigg]$$

$$\Delta P_5 = \frac{1}{Fr} \times \left[(Log(b_1(L_1 - L_{in}) + 1/\rho_{in}) - Log(1/\rho_{in}))/b_1 \right]$$

$$\Phi_5(t) = \Delta P_1 + \Delta P_3 + \Delta P_4 + \Delta P_5 + \Delta P_2 \times [A_1(N_{tpc}(1-\Delta))(\xi_1 x_1 - \xi_2 x_3)] + K_{in}\rho_{in}v_{in}^2 \quad \text{(D.5)}$$

$$\Delta P_6(t) = (M_{tpc}Log(1 + b_2(L_2 - L_1)\rho_1)((A_1 - A_2)dL_1 - A_1 dL_{in}))/b_2$$

$$\Delta P_7(t) = (Log(1 + b_2(L_2 - L_1)\rho_1))/b_2$$

$$\Delta P_8(t) = (A_2 M_{tpc}(-A_2 M_{tpc}Log(1 + b_2(L_2 - L_1)\rho_1) + b_2\rho_1(A_2 M_{tpc}(L_2 - L_1) + Log(1 + b_2(L_2 - L_1)\rho_1)v1)))/(b_2^2\rho_1)$$

$$\Delta P_9(t) = N_f \times \left[(1/(2b_2^3\rho_1^2))(2A_2^2 M_{tpc}^2 Log(1 + b_2(L_2 - L_1)\rho_1) + b_2\rho_1(A_2^2 M_{tpc}^2(L_2 - L_1)(-2 + b_2(L_2 - L_1)\rho_1) - 4A_2 M_{tpc}(Log(1 + b_2(L_2 - L_1)\rho_1) + b_2(L_1 - L_2)\rho_1)v1 + 2b_2 Log(1 + b_2(L_2 - L_1)\rho_1)\rho_1 v1^2)) \right]$$

$$\Delta P_{10} = \frac{1}{Fr} \times \left[(Log(b_2(L_2 - L_1) + 1/\rho_1) - Log(1/\rho_1))/b_2 \right]$$

$$\Phi_6(t) = \Delta P_6 + \Delta P_8 + \Delta P_9 + \Delta P_{10} + \Delta P_7 \times [A_2(N_{tpc}(1-\Delta))(\xi_1 x_1 - \xi_2 x_3)] + K_{exit}\rho_2 v_2^2 \quad \text{(D.6)}$$

$$\Phi_7(t) = \frac{\Delta P_{ext} - \Delta P_{heavy} - \Delta P_{light}}{(Log(1 + b_2(L_2 - L_1)\rho_1))/b_2 + (Log(1 + b_1(L_1 - L_{in})\rho_{in}))/b_1} \quad \text{(D.7)}$$

Putting Eq. 50 to Eq. 54 into Φ_1(t) to Φ_7(t), we found the expressions for Φ_8(t) to Φ_{12}(t).

ACKNOWLEDGMENT

The Marie Skodowska-Curie Actions Individual Fellowship grant by the European Commission's Horizon 2020 research and innovation program for the project HisTORIC (No 789476) is gratefully acknowledged.

REFERENCES

Ambrosini, W., 2009. Discussion on the stability of heated channels with different fluids at supercritical pressures. Nuclear Engineering and Design 239, 2952 – 2963.

Ambrosini, W., Sharabi, M., 2008. Dimensionless parameters in stability analysis of heated channels with fluids at supercritical pressures. Nuclear Engineering and Design 238, 1917 – 1929.

Bindra, H., Rizwan-uddin, 2014. Effects of modeling assumptions on the stability domain of bwrs. Annals of Nuclear Energy 67, 13 – 20. Advanced stability analysis for nuclear reactors.

Chatoorgoon, V., 2001. Stability of supercritical fluid flow in a single-channel natural-convection loop. International Journal of Heat and Mass Transfer 44, 1963 – 1972.

Clausse, A., Lahey, R.T., 1991. The analysis of periodic and strange attractors during density-wave oscillations in boiling flows. Chaos Solitons and Fractals 1, 167 – 178.

Dobashi, K., Oka, Y., Koshizuka, S., 1997. Core and plant design of the power reactor cooled and moderated by supercritical light water with single tube water rods. Annals of Nuclear Energy .

Dokhane, A., Hennig, D., Rizwan-uddin, Chawla, R., 2007a. BWR stability and bifurcation analysis using reduced order models and system codes: Identification of a subcritical hopf bifurcation using RAMONA. Annals of Nuclear Energy 34, 792 – 802.

Dokhane, A., Hennig, D., Rizwan-uddin, Chawla, R., 2007b. Interpretation of in-phase and out-of-phase BWR oscillations using an extended reduced order model and semi-analytical bifurcation analysis. Annals of Nuclear Energy 34, 271 – 287.

Jain, P.K., Rizwan-uddin, 2008. Numerical analysis of supercritical flow instabilities in a natural circulation loop. Nuclear Engineering and Design 238, 1947 – 1957. ICONE-14 - 14th International Conference on Nuclear Energy.

Pandey, V., Singh, S., 2016. A bifurcation analysis of boiling water reactor on large domain of parametric spaces. Communications in Nonlinear Science and Numerical Simulation 38, 30 – 44.

Pandey, V., Singh, S., 2017. Bifurcation analysis of the simplified models of boiling water reactor and identification of global stability boundary. Nuclear Engineering and Design 315, 93 – 103.

Paul, S., Singh, S., 2014a. Analysis of sub- and supercritical hopf bifurcation with a reduced order model in natural circulation loop. International Journal of Heat and Mass Transfer 77, 344 – 358.

Paul, S., Singh, S., 2014b. A density variant drift flux model for density wave oscillations. International Journal of Heat and Mass Transfer 69, 151 – 163.

Paul, S., Singh, S., 2015. Linear stability analysis of flow instabilities with a nodalized reduced order model in heated channel. International Journal of Thermal Sciences 98, 312 – 331.

Paul, S., Singh, S., 2017a. Analysis of local bifurcations in a channel subjected to non-uniform axial heating. International Journal of Heat and Mass Transfer 108, 2143 – 2157.

Paul, S., Singh, S., 2017b. On nonlinear dynamics of density wave oscillations in a channel with non-uniform axial heating. International Journal of Thermal Sciences 116, 172 – 198.

Rahman, M.E., Singh, S., 2018. Non-linear stability analysis of pressure drop oscillations in a heated channel. Chemical Engineering Science 192, 176 – 186.

Rizwan-uddin, 2006. Turning points and sub- and supercritical bifurcations in a simple bwr model. Nuclear Engineering and Design 236, 267 – 283.

Sharma, M., Pilkhwal, D., Vijayan, P., Saha, D., Sinha, R., 2009. Linear and non-linear stability analysis of a supercritical natural circulation loop, in: ICONE 17, July 12-16, Brussels, Belgium.

Sharma, M., Pilkhwal, D., Vijayan, P., Saha, D., Sinha, R., 2010. Steady state and linear stability analysis of a supercritical water natural circulation loop. Nuclear Engineering and Design 240, 588 – 597.

Singh, M.P., Rahman, M.E., Singh, S., 2018. Nodalized reduced ordered model for stability analysis of supercritical fluid in heated channel, in: Power and Energy Conference, ASME 2018, Orlando, Florida, USA.

Strogatz, S.H., 1994. Nonlinear Dynamics and Chaos. Persus book publishing.

Verma, D., Paul, S., Wahi, P., 2018. Stability and bifurcation characteristics of a forced circulation BWR using a nuclear-coupled homogeneous thermal-hydraulic model. Nuclear Science and Engineering 190, 73–92.

Wahi, P., Kumawat, V., 2011. Nonlinear stability analysis of a reduced order model of nuclear reactors: A parametric study relevant to the advanced heavy water reactor. Nuclear Engineering and Design 241, 134 – 143.

Yang, W., Zavaljevski, N., 2003. Preliminary stability analysis for supercritical water reactor, in: Global 2003, Nov 16-20, New Orleans, p. 1772.

Yang, W., Zavaljevski, N., 2005. Effects of water rods on supercritical water reactor stability, in: ICAPP 2005, May 15-19, Seoul South Korea.

Yi, T.T., Koshizuka, S., Oka, Y., 2004a. A linear stability analysis of supercritical water reactors, (I) thermal-hydraulic stability. Nuclear Science and Technology .

Yi, T.T., Koshizuka, S., Oka, Y., 2004b. A linear stability analysis of supercritical water reactors, (II) Coupled neutronic thermal-hydraulic stability. Nuclear Science and Technology .

Zhao, J., 2005. Stability Analysis of Supercritical Water Cooled Reactors. Ph.D. thesis. Massachusetts Institute of Technology.

Zhao, J., Saha, P., Kazimi, M.S., 2004a. Analysis of Flow Instabilities in Supercritical Water-Cooled Nuclear Reactors. Technical Report. Massachusetts Institute of Technology.

Zhao, J., Saha, P., Kazimi, M.S., 2004b. One dimensional thermal-hydraulic stability analysis of supercritical fluid cooled reactors, in: ICONE 12-49075, Arlington, Verginia.

Zhao, J., Saha, P., Kazimi, M.S., 2006. Coupled neutronic and thermal-hydraulic out-of-phase stability of supercritical water cooled reactors, in: ICAPP 2006, June 04-08, Reno Nevada, USA.

Zhao, J., Saha, P., Kazimi, M.S., 2007. Hot-channel stability of supercritical water-cooled reactors-I: Steady-state and sliding pressure startup. Nuclear Technology 158, 158–173.